Spring 5-10-2019

LANTHANUM-BASED PEROVSKITES AS AN EFFECTIVE ELECTROCATALYST FOR WATER SPLITTING AND ENERGY STORAGE APPLICATIONS

Xavier Martinez
xmartinez@gus.pittstate.edu

LANTHANUM-BASED PEROVSKITES AS AN EFFECTIVE ELECTROCATALYST FOR WATER SPLITTING AND ENERGY STORAGE APPLICATIONS

A Thesis Submitted to the Graduate School
in Partial Fulfillment of the Requirements
for the Degree of
Master of Science

Xavier Ruiz Martinez

Pittsburg State University

Pittsburg, Kansas

May, 2019

LANTHANUM-BASED PEROVSKITES AS AN EFFECTIVE ELECTROCATALYST FOR WATER SPLITTING AND ENERGY STORAGE APPLICATIONS

Xavier Ruiz Martinez

APPROVED:

Thesis Advisor: _____
Dr. Ram Gupta, Department of Chemistry

Committee Member: _____
Dr. Khamis Siam, Department of Chemistry

Committee Member: _____
Dr. Pawan Kahol, Department of Physics

Committee Member: _____
Dr. Anuradha Ghosh, Department of Biology

ACKNOWLEDGEMENTS

I would like to express my sincerest thanks to Dr. Ram Gupta for allowing me the opportunity to research in his lab. All his patience (which was not small) and help made it possible to find satisfaction in research and growing into a real scientist. I would like to extend my appreciation to Dr. Khamis Siam, Dr. Pawan Kahol, and Dr. Anuradha Ghosh for participating in my thesis committee. An additional special thanks to Dr. Jody Neef and also Dr. Rahul Singhal for allowing me to help with their research projects and provide data for publication. My sincere regards to Pittsburg State University Chemistry department and the Kansas Polymer Research Center. I would also like to thank members of Dr. Gupta's Light, Energy and Nanotechnology Research group, Ms. Camila Zequine, Mrs. Chen Zhao, Mr. Sanket Bhoyate, and Chunyang Zhang for their support and knowledge.

The vast majority of my appreciation, gratitude, and love goes to my eternal companion, Hannah, and my wonderful children, Lilia and Julian. They have been my greatest support, cheering section and reason for pursuing my scientific passions. I would also like to thank my extended family for their loving support and encouragement. I only hope to make them proud.

LANTHANUM-BASED PEROVSKITES AS AN EFFECTIVE ELECTROCATALYST FOR WATER SPLITTING AND ENERGY STORAGE APPLICATIONS

An Abstract of the Thesis by
Xavier Ruiz Martinez

Recent changes in global weather patterns have accented the need a shift from fossil fuels to a cleaner energy option. As part of an overall plan, hydrogen production for fuel cells offer substantial power without carbon emissions. Overall water splitting, with the aid of a low cost electrocatalyst could prove to be an abundant green fuel source. Utilizing readily available transition metals, three perovskite nanostructures were studied as a multifunctional material for hydrogen production as well as an energy storage material. $LaCoO_3$ (LCO), $LaFeO_3$ (LFO), and $LaMnO_3$ (LMO) were synthesized and characterized by X-ray diffraction (XRD) and then dip coated onto nickel foam as electrodes in a standard three electrode system. The electrochemical properties were analyzed with electrochemical impedance spectroscopy (EIS), linear sweep voltammetry (LSV), and cyclic voltammetry (CV) for its electro-catalytic activity towards both the hydrogen evolution reaction (HER) and the oxygen evolution reaction (OER) as well as its effectiveness as a supercapacitor. It was shown that electrocatalytic activity toward OER was highly dependent on the material composition. Accordingly, LFO had the lowest overpotential voltage of 316 mV at 10 mA/cm^2 compared with 376 mV (LCO) and 419 mV (LMO). Toward HER, LMO showed overpotential voltage of 176 mV at 10 mA/cm^2, while LCO and LFO showed 221 mV and 230 mV, respectively. Measured over a range of current densities, the specific capacitance of LCO remained higher (~100) F/g over LCO (~45 F/g) and LFO (~35 F/g). An altered synthetic method was employed to investigate the affects of structure directing (chelating)

agents on electro-catalytic activity. Replacement of glycine with citric acid in the synthesis process was found to improve the structure characteristics and electrochemical properties of LFO. Structural improvements for LCO and LMO were unfavorable with alteration as shown by XRD. Further investigation and understanding of structure directing agents and oxygen vacancy manipulation is needed for greater material efficiency .

Table of Contents

CHAPTER
PAGE

List of Figures

CHAPTER I

INTRODUCTION

1.1 Clean renewable energy:

In 2015, the countries of the United Nations recognized the devastating effects of climate change on world health, economies and ecosystems, and thereby formed an agreement to implement global response to this threat.[1] More recently, the United States Environmental Protection Agency, published a national climate assessment which modeled the results of both the lack of and results of increasing global greenhouse gas (GHG) mitigation. It was suggested that without action toward GHG levels, the average number of days with elevated temperatures is expected to increase, which negatively impacts mortality rates, electrical infrastructure demand, and ecosystem interactions.[2] The assessment asserts that attempts to assuage the GHG upsurge will significantly reduce or prevent incidence for all modeled sectors and such reduction benefits would be expected to rise over extended time frames. The U.S. Department of Energy has outlined 7 clean energy sources in which further investment is sought to transition to a more reliable energy sector, namely: wind, solar, water, geothermal, bioenergy, nuclear, and hydrogen/fuel cell energy.[3]

As part of the overall plan for a cleaner energy future, hydrogen production for use as a fuel for hydrogen and fuel cell powered vehicles yields highly efficient power with

little to no carbon emissions. One of the many routes to a renewable hydrogen source is the electrolysis of water or splitting of the water molecule to its base elements.

1.2 Water splitting:

Overall water splitting occurs when electric potential is applied to two half-reactions, resulting in the hydrogen evolution reaction (HER) at the cathode and the oxygen evolution reaction (OER) at the anode as shown in the following equations:[4]

$$4OH^-(aq) \rightarrow 2H_2O\ (l) + 4e^- + O_2(g) \quad (1)$$

$$4e^- + 4H_2O\ (l) \rightarrow 4OH^-(aq) + 2H_2(g) \quad (2)$$

Theoretically, this reaction requires 1.23 V (vs. RHE) to proceed, however in practical application, substantially higher potentials (overpotential) are needed to overcome the sluggish OER reaction kinetics in an alkaline solution.[5]

1.2.1 Electrocatalysts:

Lower overpotentials and much improved reaction kinetics can be achieved through utilization of a catalytic material that provide suitable surface area to promote enhanced electron transfer between the solution and electrodes. Noble, precious metals such as platinum, iridium, rhodium actively catalyze the production of hydrogen and oxygen on their surfaces, in addition to oxides of iridium and ruthenium (IrO_2, RuO_2) for the OER, as outstanding electrocatalysts.[6,7,8] Certain drawbacks such as inflated economic pricing and scarcity are apparent with these precious metal catalysts. Additional complications, which affect the overall abilities of these materials, are their susceptibility toward corrosion and cycling instability.[9]

1.3 Perovskites:

Efforts to move away from the rare, noble metals has led to the investigation of many different earth abundant, nonprecious metal oxides. After an initial start in the 1980's by Bockris and Otagawa, perovskite metal oxides have had a recent resurgence in study owing to their electronic properties applicable in a plentitude of applications.[10] Perovskite oxides of the general formula, ABO_3, where the A site is generally a group 2A or 3B cations and the B site commonly contains transition metals found in the fourth row.[11,12,13] Perovskite oxides of this type have stable surfaces which resemble the (001) plane, exposing B-site metals.[14,15] These exposed locations primarily serve as active sites for the electrocatalytic interactions of perovskite materials.

1.3.1 Crystal structure:

The perovskites of interest contained herein, are of the ABO_3 type, where lanthanum is in the A site, and three different first row transition metals (Co, Fe, Mn) are found in the B site. Perovskite metal oxides of these arrangements have been found to form a rhombohedral symmetry crystal structure where 6 oxygens surround the B-site metal in an octahedron coordination complex. Repeating octahedron units with 12 shared oxygen coordination sites, create a cavity in which the lanthanum metal can occupy, forming the perovskite structure as seen in Figure 1.3.[16,17,18] Perovskites of the ABO_3 type have been noted for their structural stability at a large temperature range due to interactions of bond distances, transition metal oxidation states and ionic radii.[19] It is these same factors that influence the formation of naturally, inherent oxygen vacancies in the perovskite crystal structure.[20]

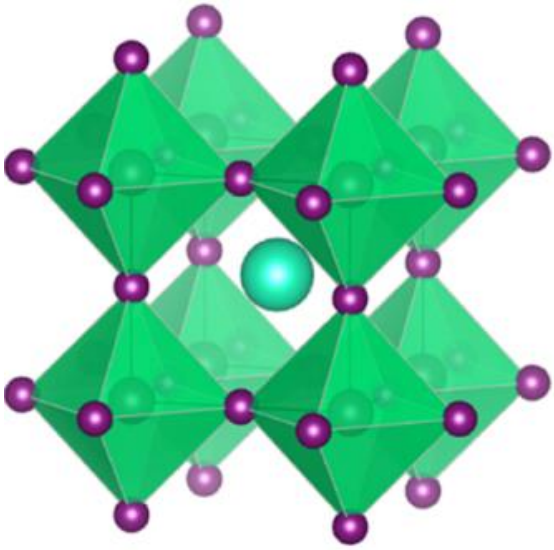

Figure 1.3. Perovskite crystal structure model.[18] Reprinted with permission from ACS publications

1.4 Electrochemical supercapacitors:

In addition to electrocatalytic water splitting abilities, perovskite metal oxides have been noted to store electrical energy through redox mechanisms with exposed surface metals and other mechanisms related to oxygen vacancies or holes in the crystalline lattice. This energy storage property has been utilized and focused in the direction of producing more efficient electrochemical supercapacitor devices. An electrochemical supercapacitor blends characteristic properties of both traditional capacitors and cell batteries namely: higher power densities than batteries, but less than capacitors and higher energy density than capacitors but generally less than that of batteries.[21] Attractive attributes such as sustainability, long recyclability life, wide operating temperature ranges, fast charging rate

and environmentally friendly are dependent on active material used for electrode construction.[22] Material charge storage mechanisms are divided into two distinct categories: electrical double-layer capacitance (EDLC), which develops an accumulation of charge between the material surface and the electrolyte, and pseudo-capacitance established by faradic reactions or ion intercalation processes at active sites on the electrode material's surface.[23] Electrochemical supercapacitors are beginning to find application in earth friendly electric vehicles, a wide variety of electric devices and large grid energy storage systems for renewable sourced power.

1.5 Multifunctional material:

The primary focus of this work was to investigate and compare electrochemical properties of three lanthanum-based perovskite metal oxides as multifunctional materials. Materials that could offer functionality as an electrode for both OER and HER which lowers overpotentials and could be constructed from readily available, economical starting materials is highly sought after.[24,25] In addition to serving as both anode and cathode in water splitting applications, this low cost multipurposed material could be utilized as an energy storage device with good specific capacitance, high energy/power density and excellent electrochemical stability. To this end, $LaCoO_3$ (LCO), $LaFeO_2$ (LFO) and $LaMnO_3$ (LMO) were analyzed as viable options for OER, HER, and supercapacitor electrode materials.

CHAPTER II

EXPERIMENTAL DETAILS

2.1 Materials:

Perovskite metal oxides were synthesized from the nitrates of the transition element precursors, namely: lanthanum(III) nitrate hexahydrate, 99.9% (Strem Chemicals, Inc. Newburyport, MA, USA), cobalt(II) nitrate hexahydrate, 99% (Strem Chemicals, Inc. Newburyport, MA, USA), iron(III) nitrate nonahydrate 99+% (Acros Organics, New Jersey, USA), and manganese (II) nitrate tetrahydrate, 97.0% (Sigma-Aldrich, St. Louis, MO, USA). To aid in the synthetic process, gylcine, 99% (Sigma-Aldrich, St. Louis, MO, USA), anhydrous citric acid, 99.5% (Acros Organics, New Jersey, USA), and polyvinylpyrrolidone (PVP), MW 58,000 (Acros Organics, New Jersey, USA) were used as structure directing and surfactant agents. Portions of ammonium hydroxide, 29% (Fisher Scientific, Pittsburgh, PA, USA) were used to control pH of reaction solution. Fabrication process of electrodes involved the use of nickel foam substrates, acetylene black, polyvinylidenedifluoride (PVDF) and 1-Methyl-2-pyrrolidinone (NMP), all from MTI Corporation (Richmond, CA, USA).

2.2 Synthetic process:

LCO was synthesized by sonicating 0.3 g of PVP and 0.9 g of glycine in 15 mL of deionized water for ~15 min until solids were dissolved. Two solutions of $La(NO_3)_3 \cdot 6H_2O$ (0.4 g) in deionized water (10 mL) and $Co(NO_3)_3 \cdot 6H_2O$ (0.4 g) in water (10 mL) were then added to the glycine mixture. 320 µL of NH_4OH (29%) was added to bring solution to a pH of 9.0. The mixture was divided into two Parr reactors (45 mL) and heated for 12 h at 180 °C. Solid precipitate was washed (deionized water) and centrifuged (10 min, 1,000 rpm), then dried overnight at 60 °C. The material was ground in a mortar and pestle, transferred to kiln in a ceramic boat dish and heated to 600 °C (5 °C/min) for 2 h in air. Formation of porous material was accomplished by a second heating at 650 °C (5 °C/min) for 2 h. LFO and LMO were synthesized in similar manner with an additional 320 µL of NH_4OH added to LFO for adjusting solution pH to 9.0.

2.2.1 Alternative synthesis with citric acid:

As a study of the effects of structure directing agents, citric acid was used as a substitute for glycine in the previous synthetic method. LCO, LFO and LMO were synthesized by combining 5 mmol of citric acid with 0.3 g of PVP and sonicating in 15 mL of water until well dissolved. To the citric acid solutions, 2 mmol of lanthanum nitrate in 10 mL of water and 2 mmol portions of nitrates of cobalt, iron and magnesium in water (10 mL) were added. Solutions were transferred directly to Parr reactors and heated to 180 °C for 12 h. Resulting precipitates were decanted and washed with water and centrifuged (10 min, 1,000 rpm) three times. After drying at 60 °C, overnight, the powdered material was transferred to a ceramic boat and calcinated according to the same process as previously

mentioned (600 °C (5 °C/min) for 2 h in air, then 650 °C (5 °C/min) for 2 h).

2.3 X-ray diffraction spectroscopy:

After synthesis and calcination, a Shimadzu XRD-6000 X-ray diffractometer ($CuK\alpha_1$ (λ=1.5406 Å), 2θ-θ mode) was utilized to evaluate phase planes. As incident X-ray radiation passed over the powdered perovskite materials, a 0.2 mm slit receiving detector collected diffraction rays from the rotating stage a 2θ range of 10-80 degrees.

2.4 Scanning electron microscopy:

Perovskite particle size and topography were analyzed with a JEOL JSM-840A scanning electron microscope at the University of Kansas with the help of Xianglin Li. Due to low electrical conductivity of the material, the powdered materials were sputter coated in gold to improve conductivity and remove charging effects.

2.5 Electrochemical method for water splitting and supercapacitor analysis:

2.5.1 Perovskite material on nickel foam substrate electrodes:

Perovskite metal oxide electrodes were prepared by dip coating metal oxide solution on a nickel foam substrate. Six nickel foams, for each perovskite, of roughly the same dimensions were cut and sonicated in 1M hydrochloric acid for 10 min. Foams were rinsed thrice in water and sonication until pH was measured neutral. Foams were quick dried with compressed air and placed in a vacuum oven for 30 min (70°C). Meanwhile, 1-methyl-2-pyrrolidinone was added dropwise (~20 drops) to PVDF binder (2 mg) and heated at 60 °C for 5 min or until fully dissolved. To the binder solution, 2 mg of acetylene

black and 16 mg of each perovskite was added and mixed well in sonicator for 30 mins with intermittent agitation throughout. Foam substrates were dipped in metal oxide solutions and hung in vacuum oven rack to dry (24 hr) forming 80% perovskite electrodes.

2.5.2 Electrochemical analysis cell:

Electrocatalytic activity toward OER, HER and supercapacitor capabilities of LCO, LFO, and LMO were electrochemically measured with a Versastat 4-500 electrochemical workstation (Princeton Applied Research, USA). For OER and HER, a standard three electrode system consisting of a platinum counter electrode, saturated calomel electrode (SCE) reference electrode, and perovskite coated Ni foam working electrode in alkaline solution (1M KOH) was used as shown in Figure 2.5. The same general electrode setup was utilized for supercapacitor measurements in a 3M KOH solution.

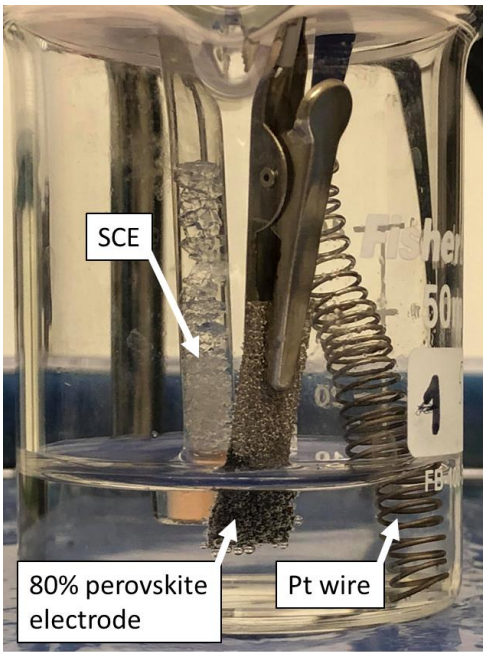

Figure 2.5. Electrochemical analysis cell.

CHAPTER III

RESULTS AND DISCUSSION

3.1 Characterization of initial synthesized perovskites:

3.1.1 X-ray diffraction analysis:

Powdered perovskite samples were examined by XRD analysis producing the spectra shown in Figure 3.1. All three perovskite spectra show characteristic perovskite crystal structure peaks, which Miller indices are labeled from the JCPDS files for LCO and LMO.[26,27] Most notable is the (110) plane at around 32˚, which is prominent on perovskites of the ABO_3 structure. Phase mixing of La_2O_3 was detected in all samples as indicated by green dots in Figure 3.1.[16,27,28] Nyamdavaa et al. showed through temperature studies, La_2O_3 phases could be minimized through increased calcination temperatures.[14] Other studies show pure phase spectra at much higher temperatures, also, however use of calcination temperatures higher than 650 ˚C would be counterproductive to the desired low cost, green end product.[29]

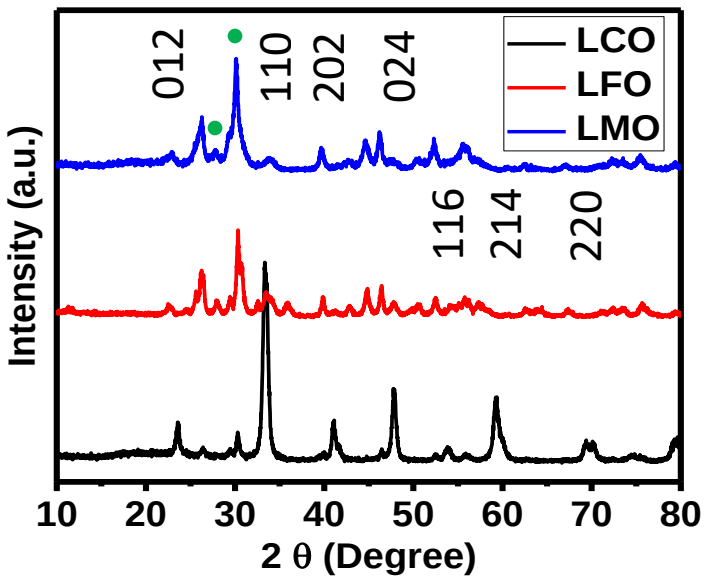

Figure 3.1: X-ray diffraction spectra with signature perovskite planes and green La_2O_3 phase markers

3.1.2 Scanning electron microscopy (SEM):

Lanthanum cobaltite nanospheres of about 100 nm are shown in Figure 3.2. The spheres covered all surfaces of larger particles providing ample surface area for electrocatalytic interactions. The copious coverage of well-formed perovskite nanospheres could likely account for the purer phase and sharper peaks in the corresponding XRD spectra.

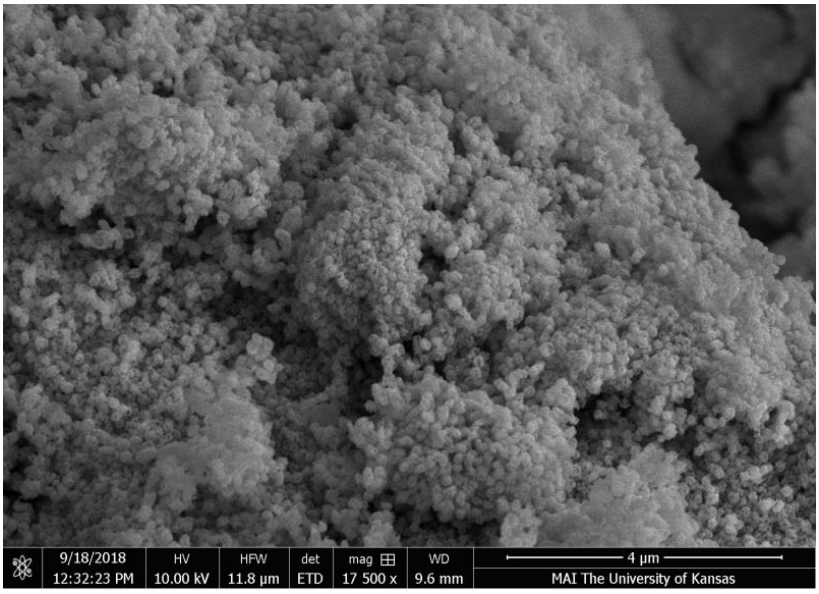

Figure 3.2: SEM image of LCO sphere-like particles

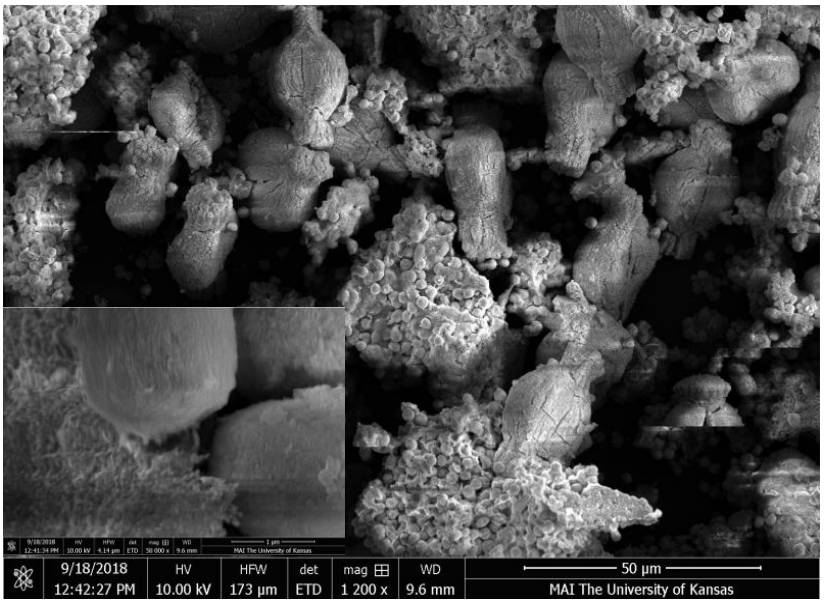

Figure 3.3: SEM image of LFO particles with 50k magnification inset

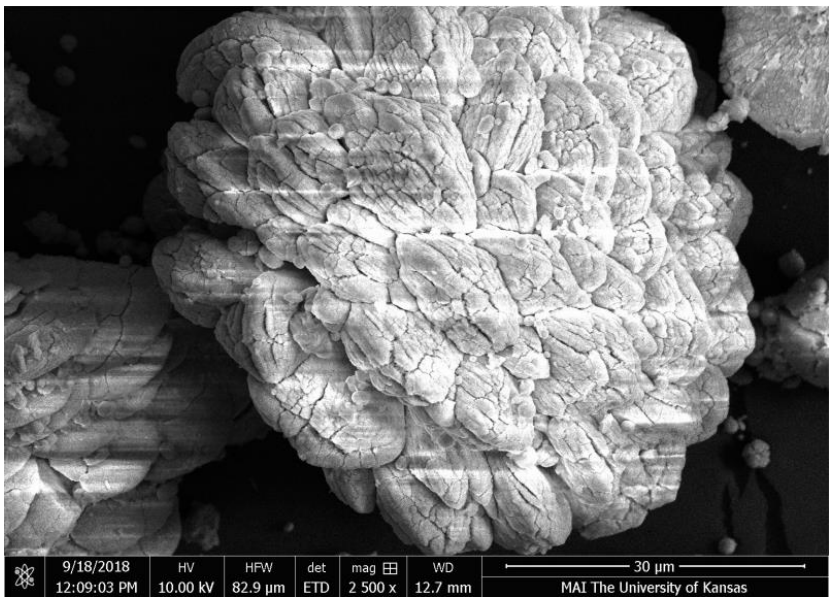

Figure 3.4: SEM image of LMO cluster type particles

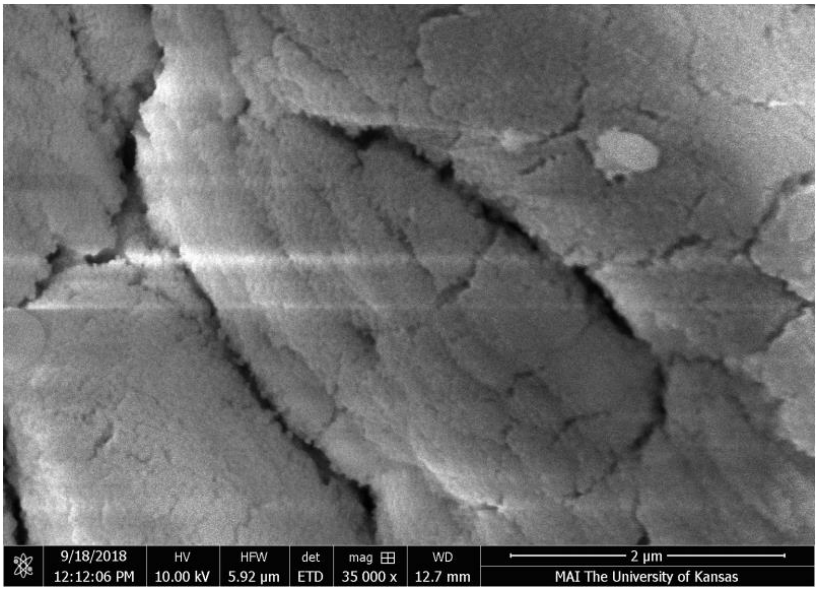

Figure 3.5: SEM image of small spheres in surface fissures

Partial coverage of larger, roughly 1 μm, sphere-like particles of LFO are shown in Figure 3.3. Smaller sized particles, less than 100 nm, were observed at higher magnification (inset) surrounding the larger orbs as well as on the surface of largest non-sphere particles. Excellent electrochemical and catalytic properties are attributed to the high and varied surface areas of the material.

Lanthanum manganese oxide particles of a different morphology are apparent in Figure 3.4. With the fewest sphere-like particles, sparsely scattered over a large disk-like cluster particles with a rough surface and many ridges, LMO looked most dissimilar to LCO and LMO at lower magnification. However, at 35,000 times magnification, very small orbs can just be seen on the edges of the crevasses that are streaked across the surface of the cluster (Figure 3.5). Even with the gold coating and high magnification, particle shape is tough to decipher, but estimated to be less than 20 nm is size.

3.2 Electrocatalytic analysis for OER:

3.2.1 Linear sweep voltammetry and Tafel analysis:

Activity toward OER was investigated by linear sweep voltammetry (LSV) for each material, as shown in Figure 3.6 from 1.0 – 1.7V. Compared at 10 mA/cm^2, onset potentials were iR corrected and shown that LFO had the lowest overpotential of 316 mV. LCO and LMO displayed overpotentials of 376 and 419 mV, respectively. These results are notable in that they deviate from perovskite electrocatalytic overpotential trends of $LaCoO_3 > LaFeO_2 > LaMnO_3$.[6,30] This trend echoing the effects of increasing d orbital electrons and bond strength of B-site transition metals with adsorbed electrolyte species.[31]

The same trend divergence is evident in comparison of Tafel slopes as shown in Figure 3.7. LFO had the lowest slope value, but LMO exhibited a lower slope than LCO. From these low slope values, all three materials proved efficient electrocatalysts for the OER however, LFO exhibited both the lowest overpotential and Tafel slope.[32] Tafel slope values in these ranges have been found to correspond to adsorbed hydroxide (Eq. 4) at the metal active sites on the perovskite surface. OER mechanism reactions could be broken down into the following equations:

$$M + OH^- \rightleftharpoons MOH + e^- \quad (3)$$

$$MOH + OH^- \rightleftharpoons MO + H_2O + e^- \quad (4)$$

$$MO + OH^- \rightleftharpoons MOOH + e^- \quad (5)$$

$$MOOH + OH^- \rightleftharpoons MOO^- + H_2O \quad (6)$$

$$MOO^- \rightleftharpoons M + O_2 + e^- \quad (7)$$

where M signifies the active site on the electrode surface.[33,32] Trend aberration and enhanced electrocatalytic activity of LFO could be accredited to desultory crystalline structure defects, requiring further investigation. Defects and deficiencies in the crystal lattice has been noted to improve such abilities toward both the oxygen reduction reaction as well as the OER.[34-35]

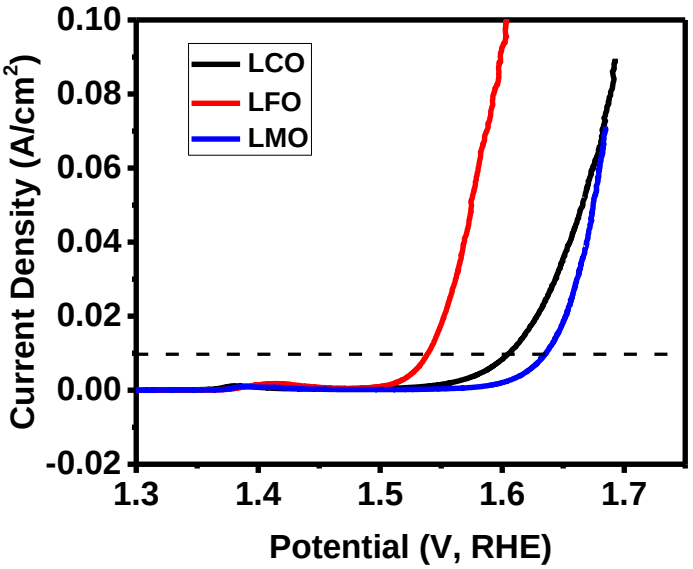

Figure 3.6: LSV polarization curves of perovskites

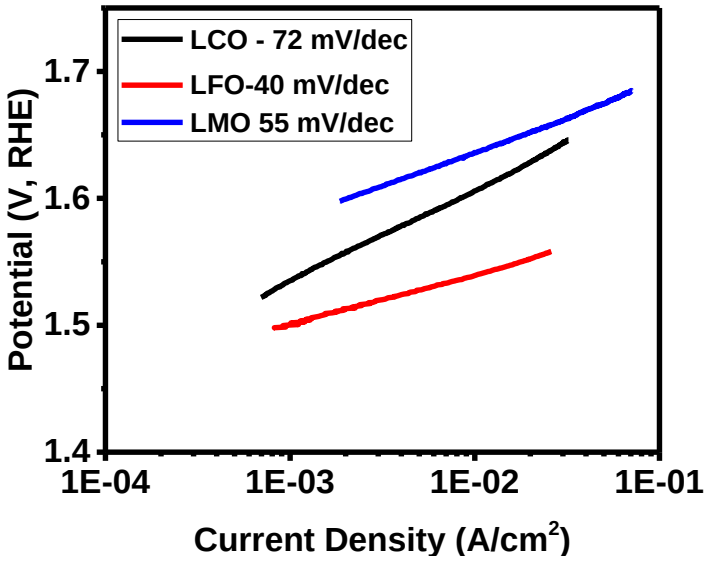

Figure 3.7: Tafel slopes for three perovskites

3.2.2 Electrochemical impedance spectroscopy:

EIS Nyquist plots of the three compounds were compared in Figure 3.8 and 3.9. At 0V LCO and LFO had similar trajectory, but showed major charge transfer impedance differences at 0.5V. From the inset, LFO measured ~2Ω, compared with LCO (~22Ω) and LMO (~100Ω). For LFO, both charge transfer resistance (Fig. 3.10) and overall resistance (Fig. 3.11) decreased with increasing voltage.

Similarly, EIS Nyquist data for LCO and LMO shown in Figure 3.12 and 3.13, respectively.

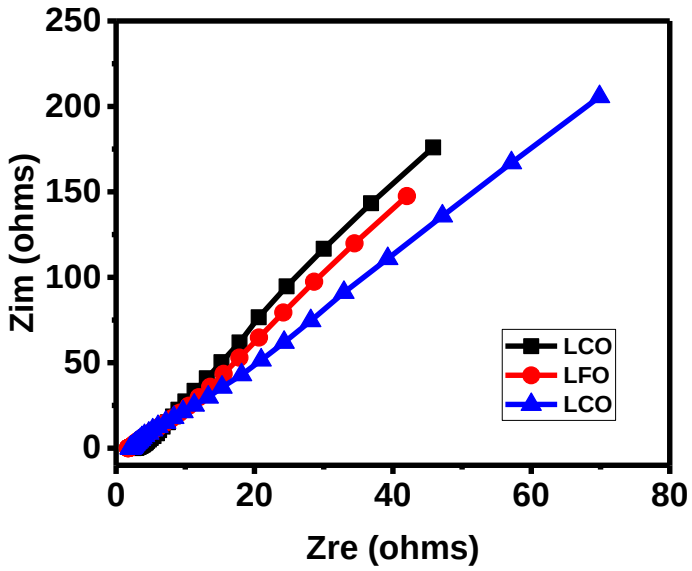

Figure 3.8: EIS Nyquist plots of perovskites at 0V

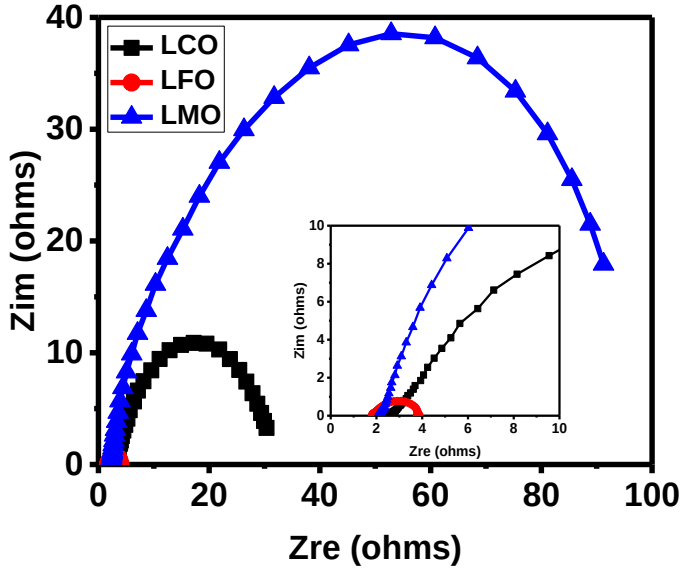

Figure 3.9: EIS Nyquist plots of perovskites at 0.5V

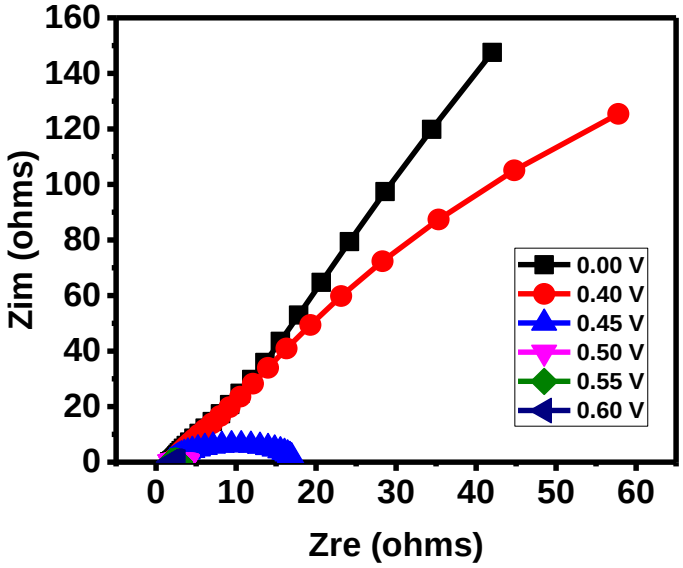

Figure 3.10: EIS Nyquist plots of LFO at various potentials

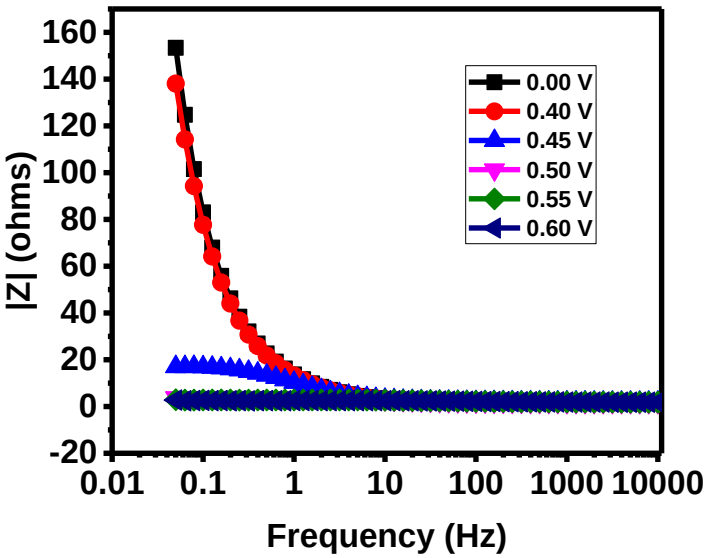

Figure 3.11: EIS Bode plots of LFO at various potentials

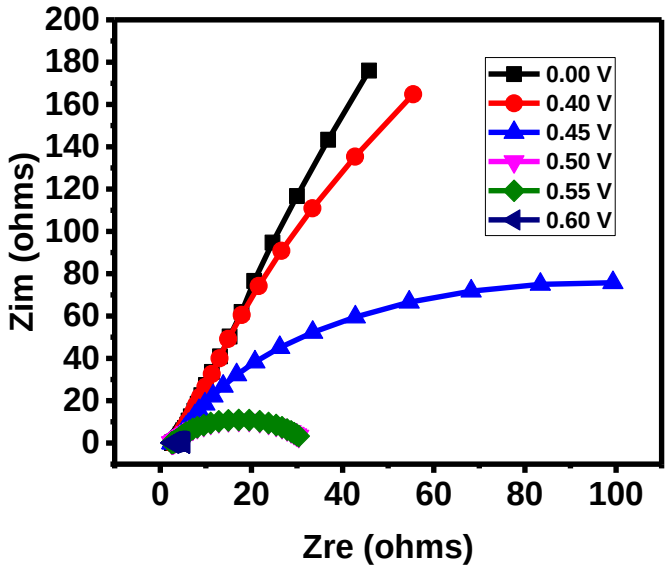

Figure 3.12: EIS Nyquist plots of LCO at various potentials

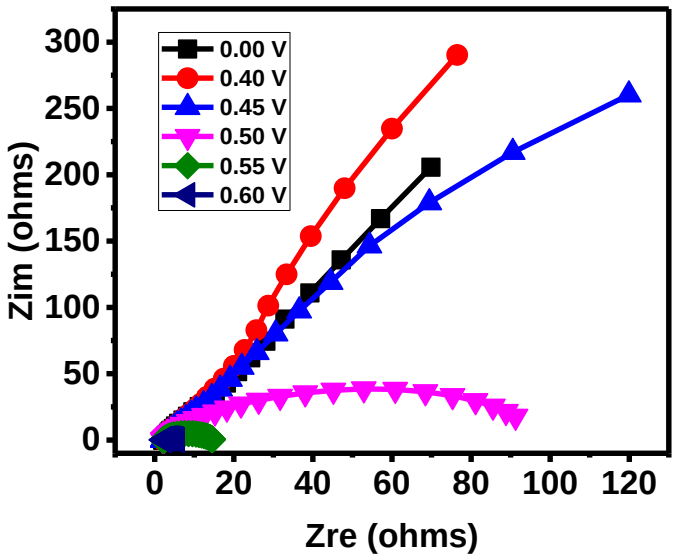

Figure 3.13: EIS Nyquist plots of LMO at various potentials

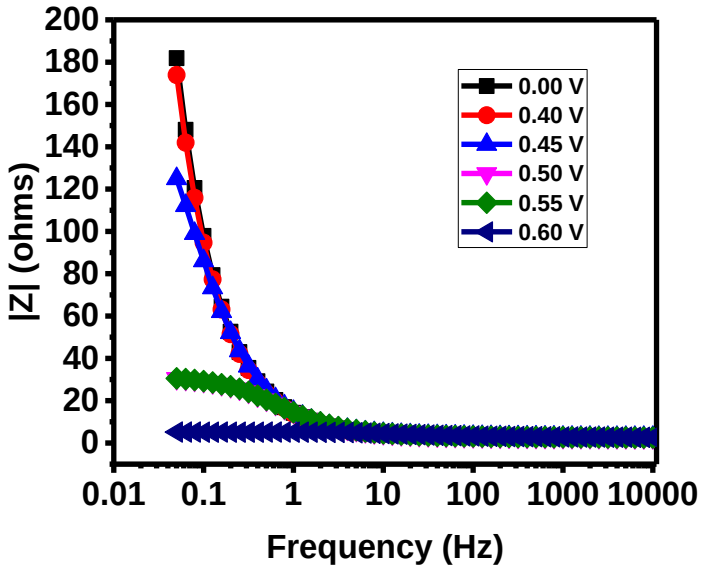

Figure 3.14: EIS Bode plots of LCO at various potentials

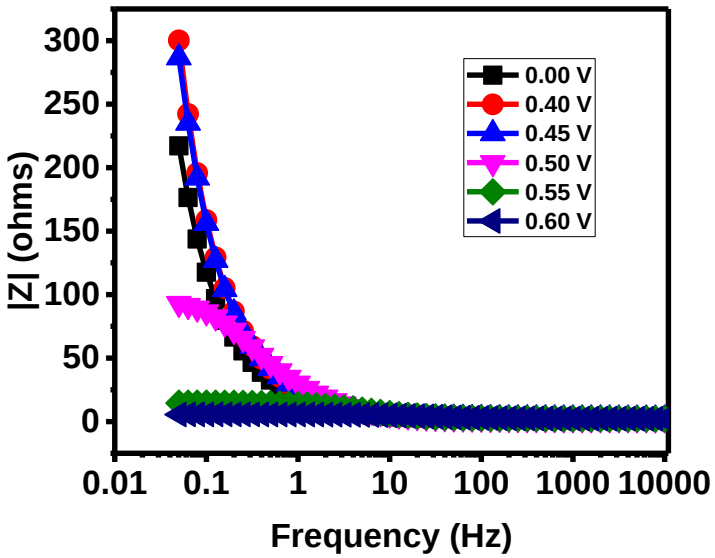

Figure 3.15: EIS Bode plots of LMO at various potentials

Additionally, EIS Bode plots for LCO are displayed in Figure 3.14, and Bode graphs for LMO are in Figure 3.15. All three materials follow the same pattern of decreasing resistance as potential increases.

3.2.3 Stability measurements:

The durability of the perovskite metal oxides was investigated by cycling CV at 300 mV/s and measuring with LSV and EIS before and after stability analysis. From the polarization curves for 1st and 2000th cycles, onset potentials remained relatively constant as seen in Figure 3.16 for LFO and Figure 3.17 for LCO. Slightly more variation in LMO, as apparent in Figure 3.18. Similar results with EIS Nyquist plots show minimal variation at both 0V and 0.5V potential ranges (Figures 3.19-3.24).

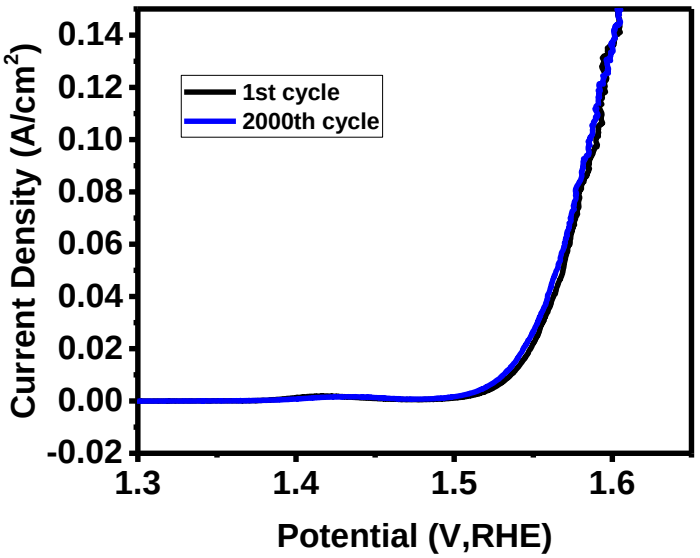

Figure 3.16: LSV stability of LFO

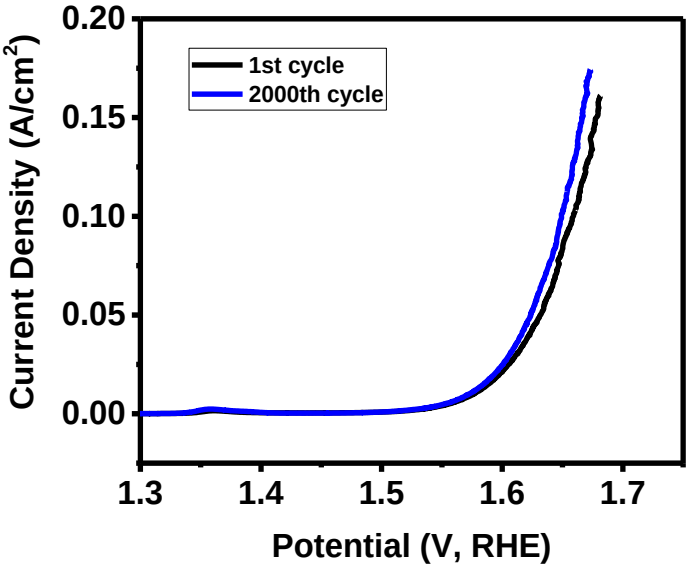

Figure 3.17: LSV stability of LCO

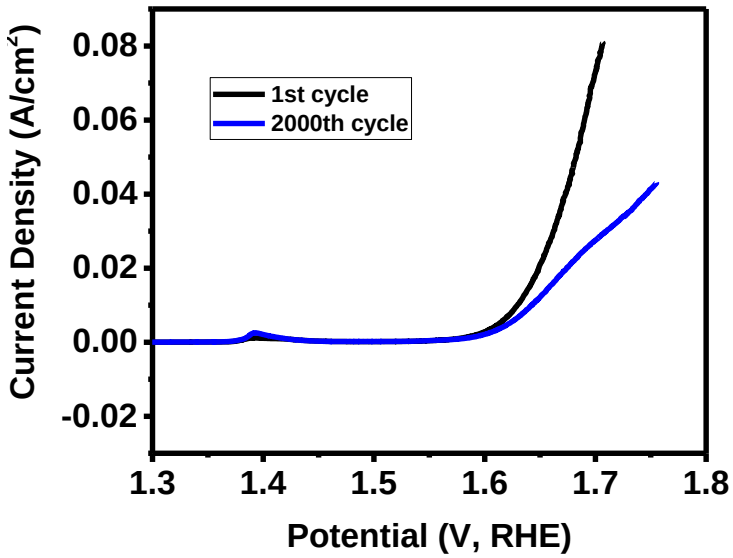

Figure 3.18: LSV stability of LMO

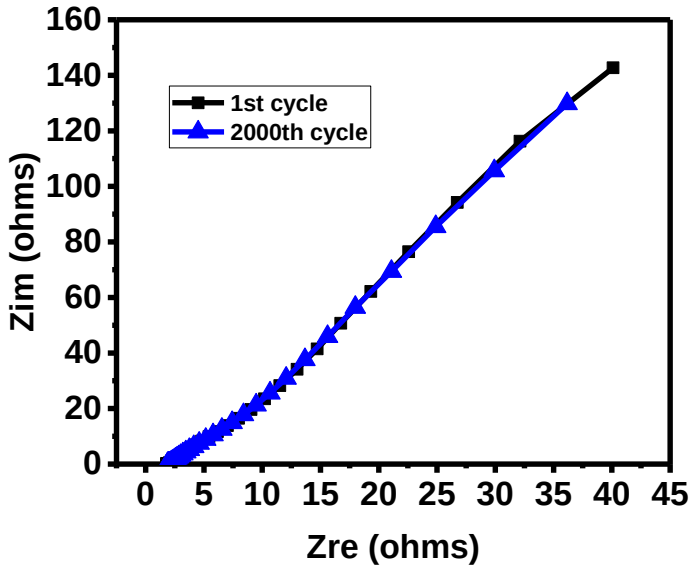

Figure 3.19: EIS Nyquist stability plots of LFO at 0V

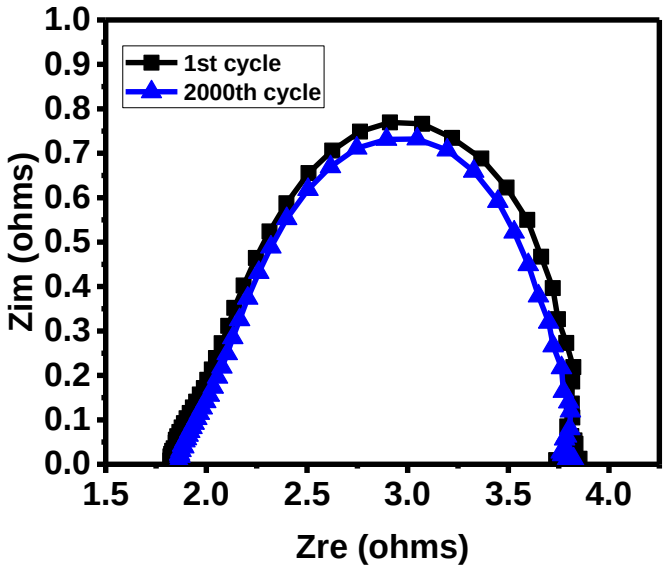

Figure 3.20: EIS Nyquist stability plots of LFO at 0.5V

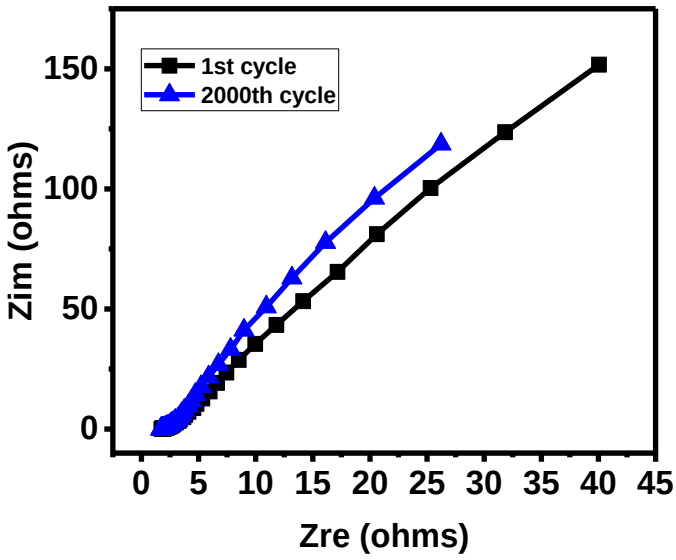

Figure 3.21: EIS Nyquist stability plots of LCO at 0V

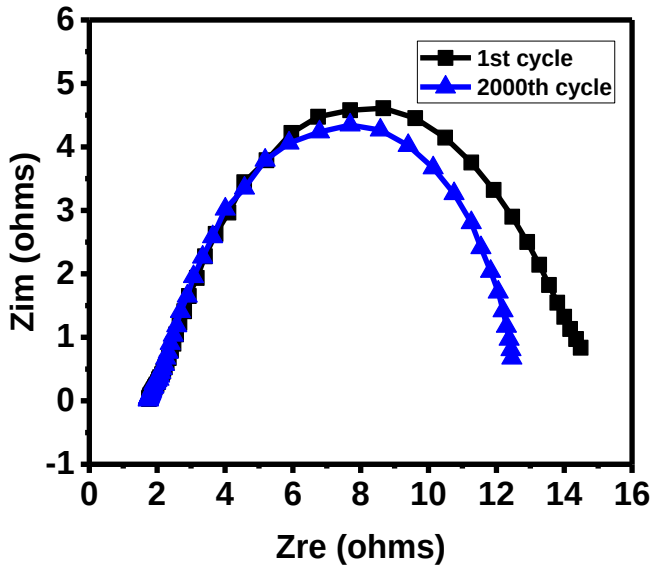

Figure 3.22: EIS Nyquist stability plots of LCO at 0.5V

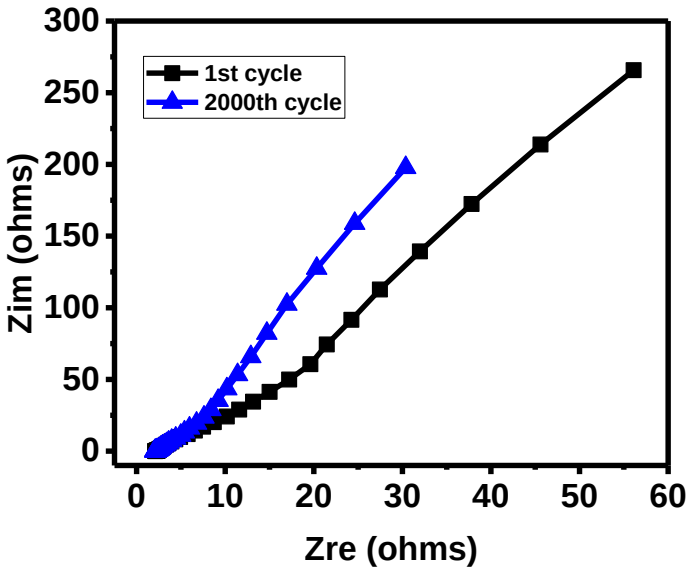

Figure 3.23: EIS Nyquist stability plots of LMO at 0V

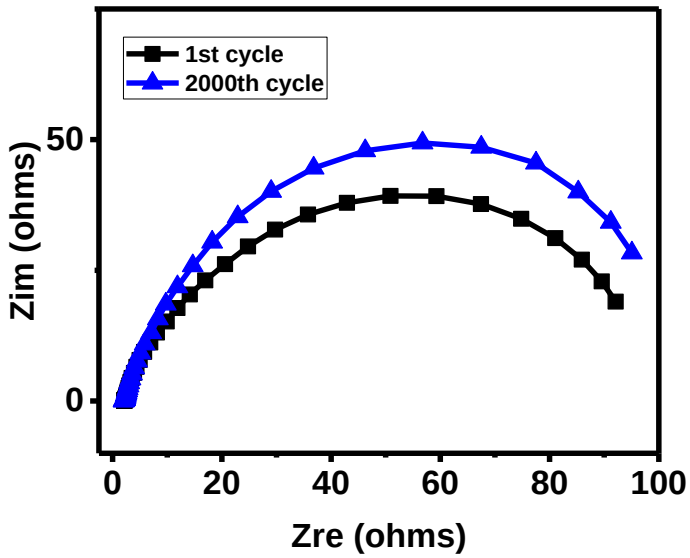

Figure 3.24: EIS Nyquist stability plots LMO at 0.5V

Additionally, chronoamperometry was utilized to evaluate the stability of the materials from the change of current density over time as seen in Figure 3.25-3.27. For LFO, current density decayed by ~15 mA/cm^2 (Fig.3.25), which indicated excellent structural stability of the electrode over a fifteen-hour test period. The LCO electrode produced a slightly smaller decay in current density of close to 6 mA/cm^2 as seen in Figure 3.26. LMO however, stayed quite consistent for over 20 hours of testing (Fig.3.27).

From the lower overpotentials, faster mechanism kinetics, lower charge transfer and overall resistance, LFO exhibited better electrocatalytic activity toward OER than LCO and LMO, as well as proved high resilience over extended use.

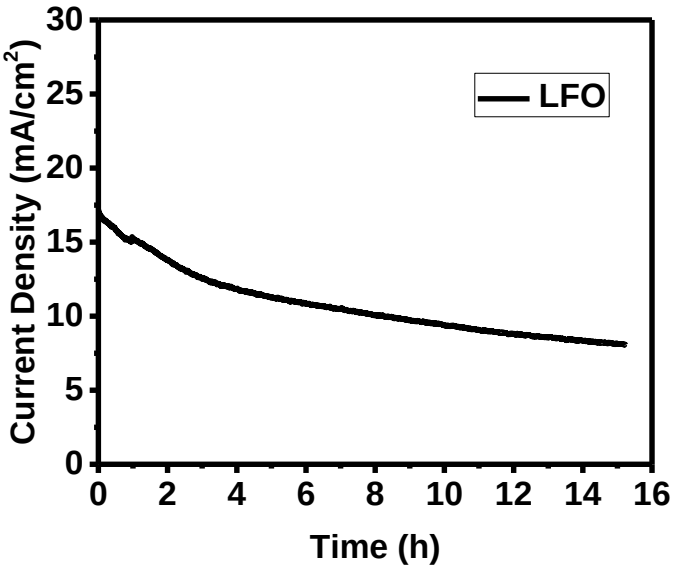

Figure 3.25: Cottrell plot of lanthanum ferrite

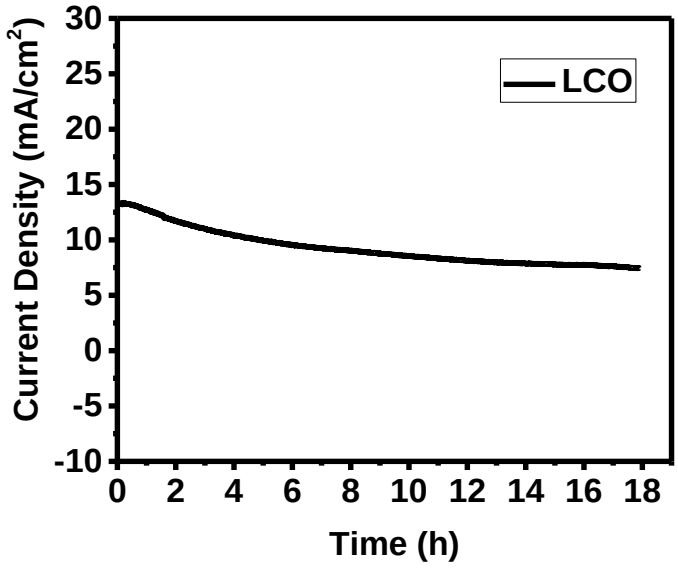

Figure 3.26: Cottrell plot of lanthanum cobaltite

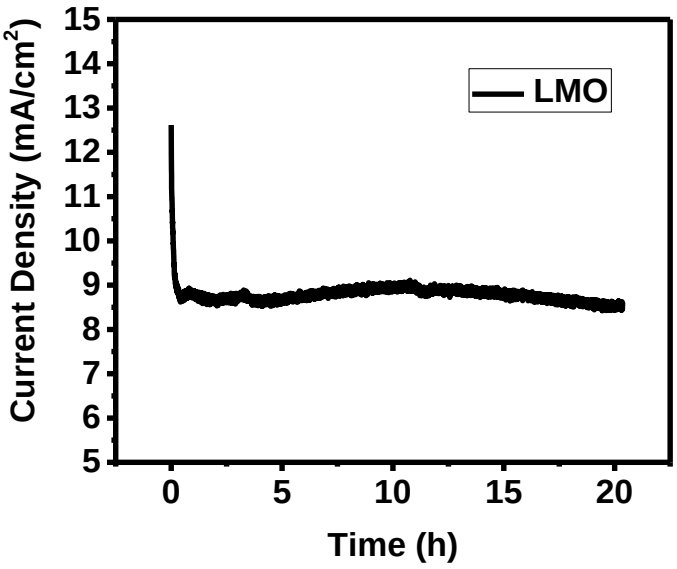

Figure 3.27: Cottrell plot of lanthanum manganite

3.3 Electrocatalytic analysis for HER:

3.3.1 Linear sweep voltammetry and Tafel analysis:

Using the same three synthesized materials, investigation into the electrocatalytic behavior toward HER was conducted in similar manner to the OER. LSV was measured from -0.9 to -1.6 V and found that LMO was calculated to have the lowest overpotential compared to LCO and LFO at 10 mA/cm^2 (Fig.3.28).

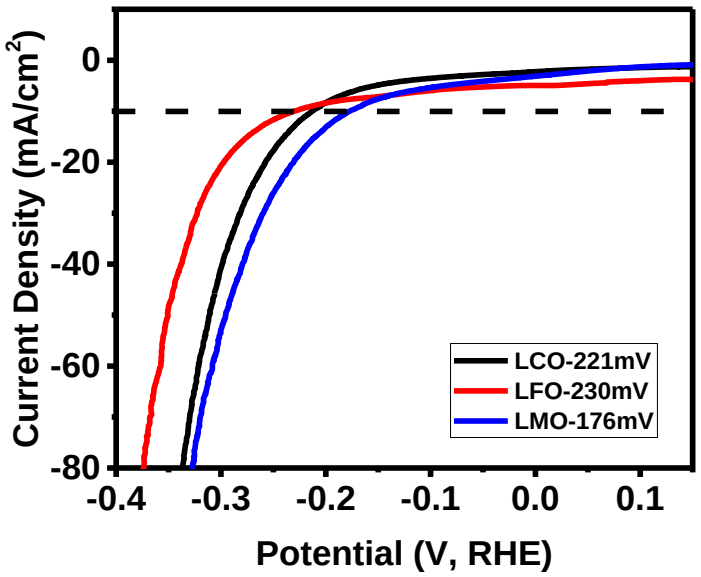

Figure 3.28: LSV polarization curves of perovskite metal oxides

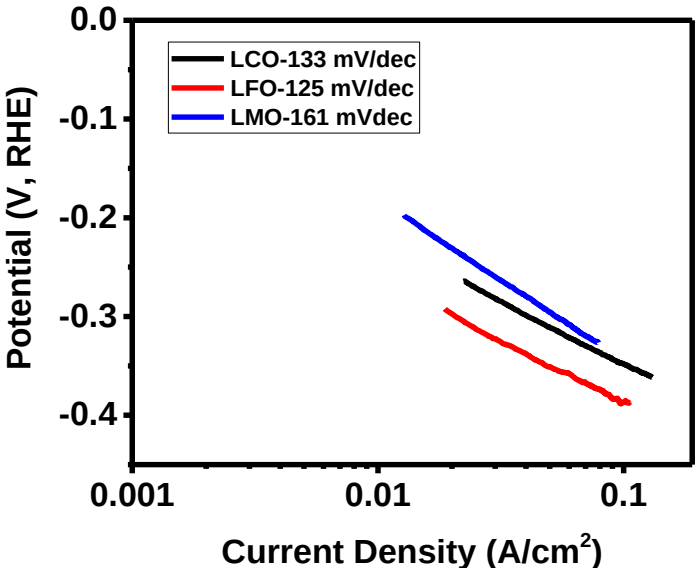

Figure 3.29: Tafel slopes for the three perovskites

3.3.2 Electrochemical Impedance Spectroscopy:

Higher Tafel slope value of LMO shown in Figure 3.29 correlate to the large transfer resistance from EIS data at 0V (Figure 3.30) indicating slower mechanistic kinetics. However, as the HER reaction proceeded at higher voltage, shown in Figure 3.31, the resistance of LMO decreased.

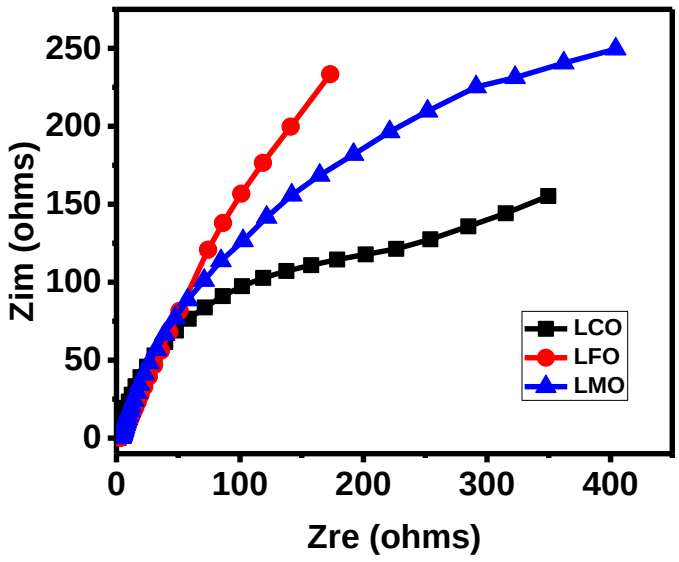

Figure 3.30: EIS Nyquist plots of perovskites at 0V

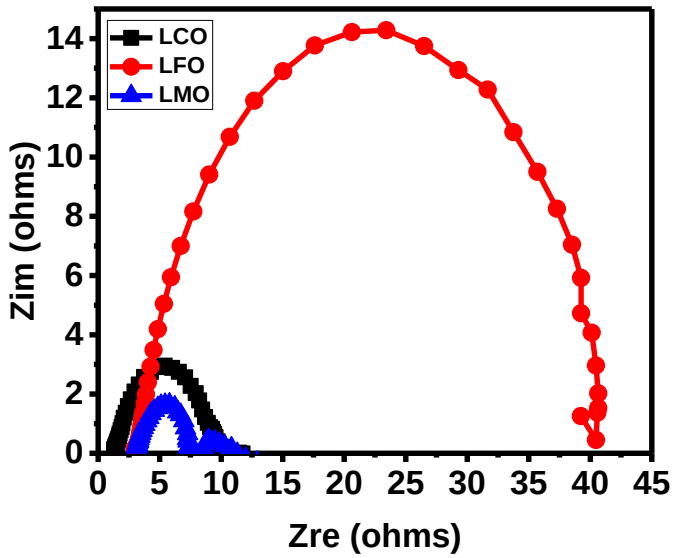

Figure 3.31: EIS Nyquist plots of perovskites at 1.3V

3.3.3 Stability measurements:

Sturdiness of the perovskite material usage was analyzed with LSV and EIS by cycling for 2,000 cycles as shown in Figures 3.32 to 3.40. All three perovskite materials performed with excellent stability with minimal deviation over the examination interval. This electrode stability is likely attributed the perovskite-type crystal structure being highly stable and therefore not affected by the alkaline environment.[36]

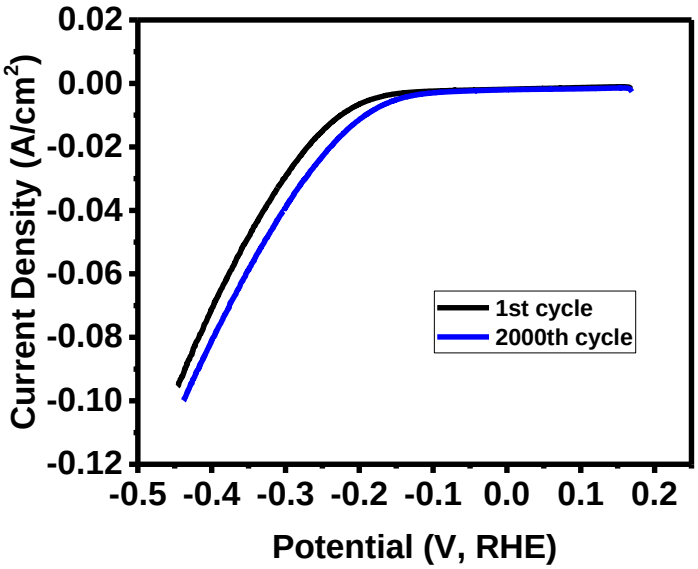

Figure 3.32: LSV stability of LMO

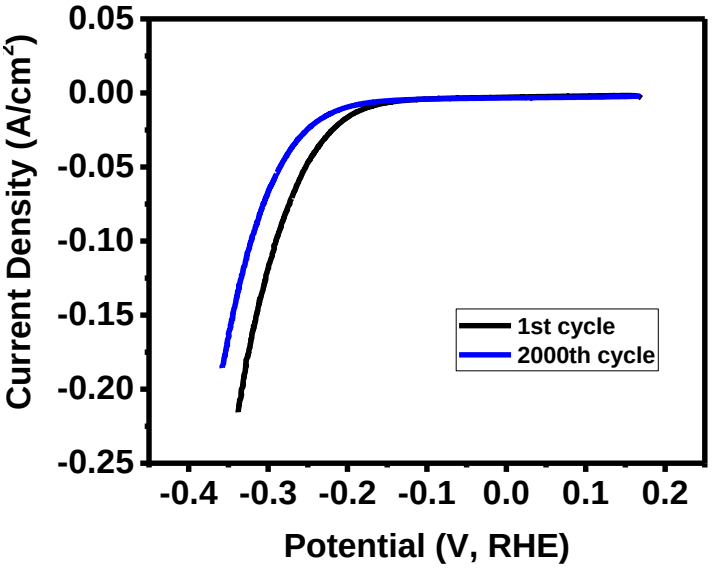

Figure 3.33: LSV stability of LCO

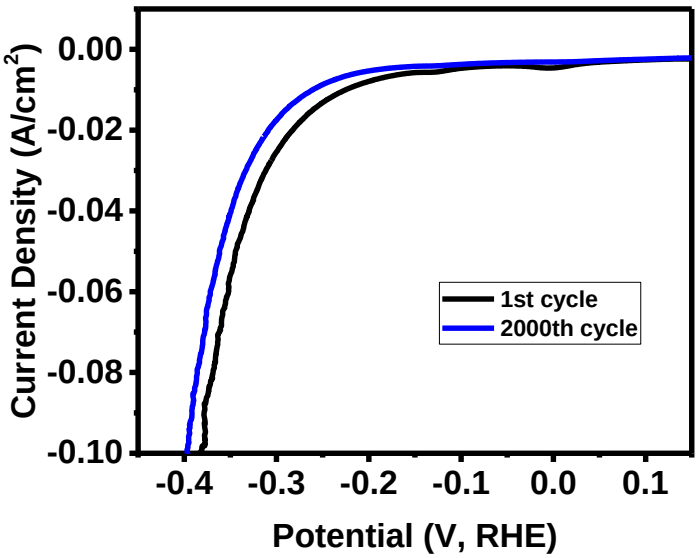

Figure 3.34: LSV stability of LFO

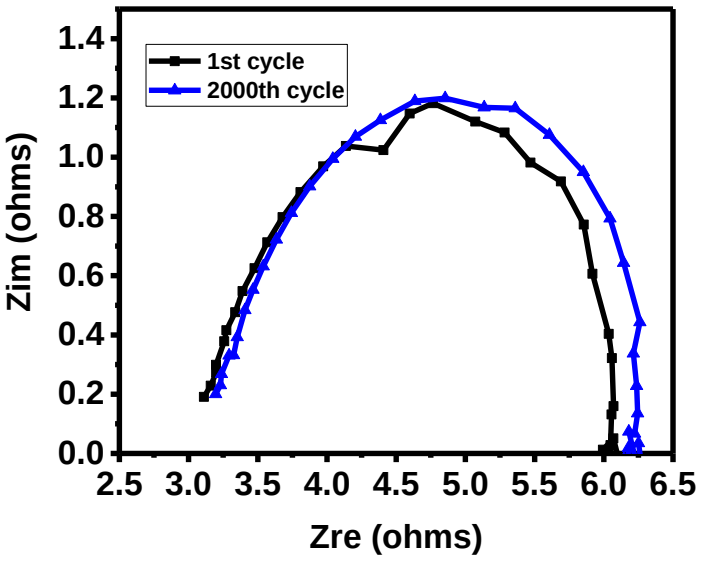

Figure 3.35: EIS Nyquist stability plots of LMO at 1.3V

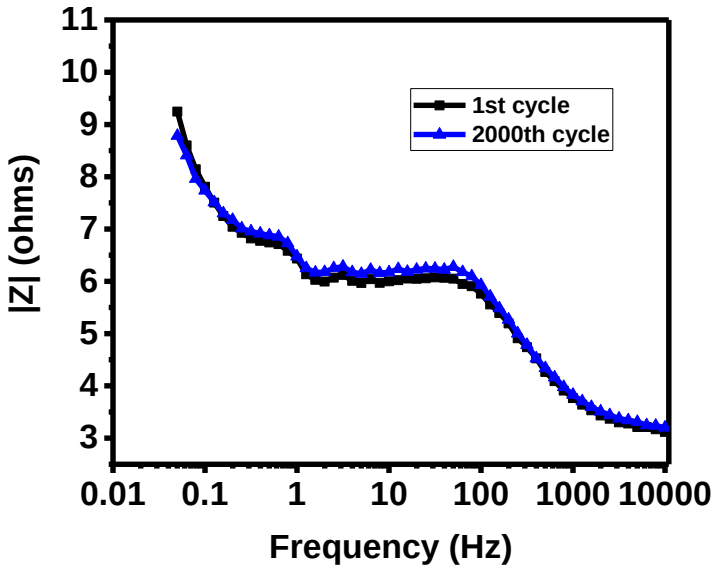

Figure 3.36: EIS Bode stability plots of LMO at 1.3V

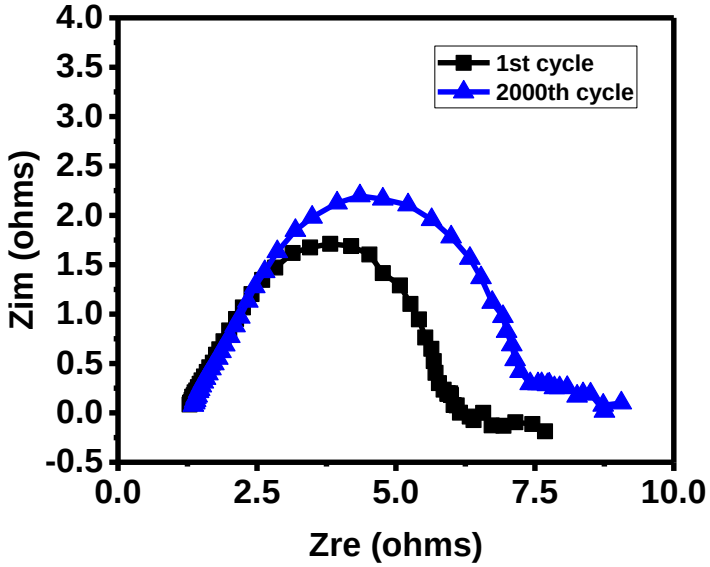

Figure 3.37: EIS Nyquist stability plots of LCO at 1.3V

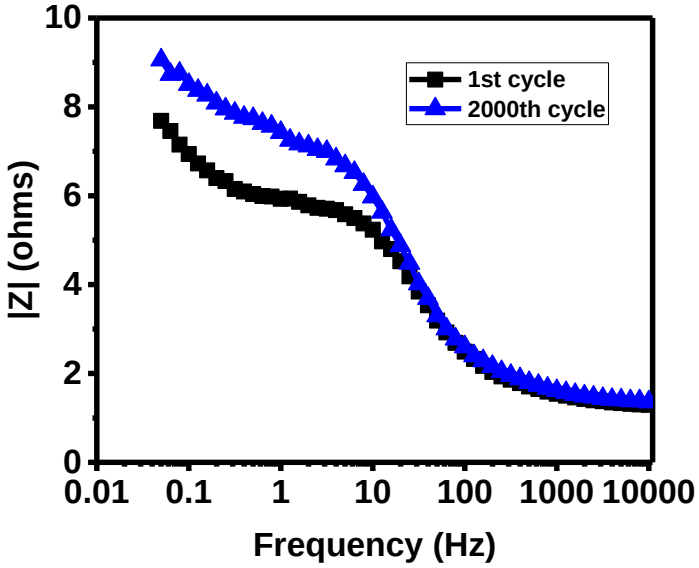

Figure 3.38: EIS Bode stability plots of LCO at 1.3V

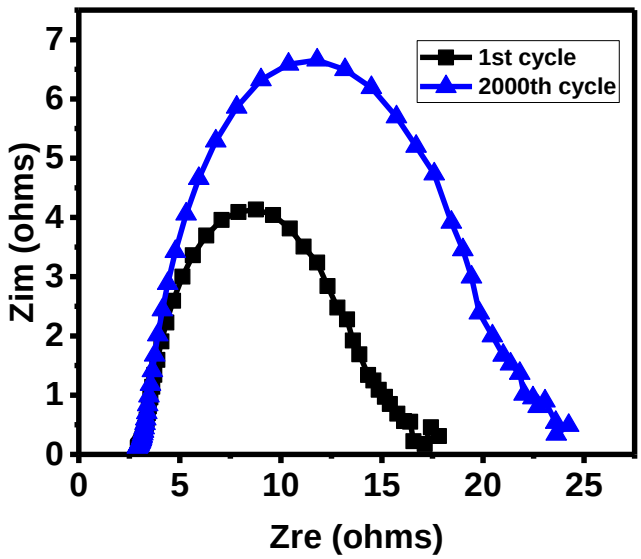

Figure 3.39: EIS Nyquist stability plots of LFO at 1.3V

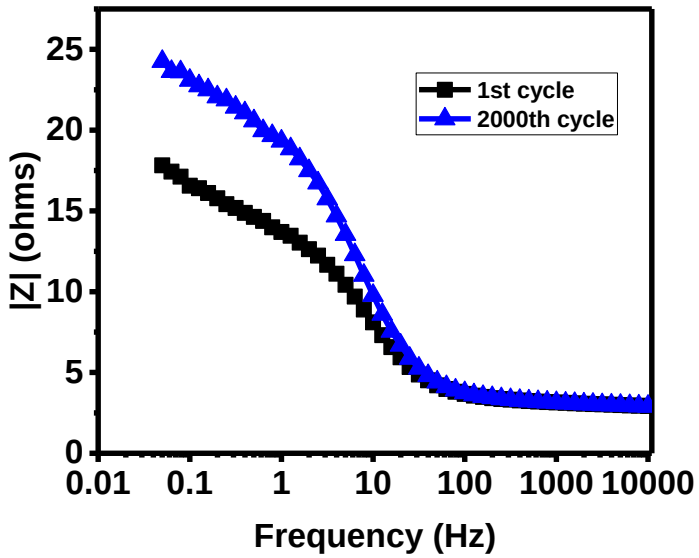

Figure 3.40: EIS Bode stability plots of LFO at 1.3V

3.4 Electrochemical properties for supercapacitors:

In effort to determine whether these specific electrocatalytic materials possessed capabilities of a truly multifunctional material, supercapacitor properties were investigated through cyclic voltammetry (CV) and galvanostatic charge-discharge (GCD) analysis at various scan rates and current densities, respectively.

3.4.1 Cyclic voltammetry:

The cyclic voltammograms shown in Figures 3.41-3.43. depict curves characteristic to materials that store energy through faradic electron charge transferring mechanisms.[22,37] Specific capacitance values for each perovskite were calculated from the voltammograms by the following:

$$C_{sp} = \frac{Q}{m\Delta V} \tag{8}$$

where Q is the area under the CV curve, m is the mass of the perovskite oxide on electrode, and ΔV is the potential window.[38] Figure 3.44 shows the comparison of specific capacitance values at scan rates between 1 and 300 mV/s. At the lower scan rates capacitance values rise sharply in all materials with LFO peaking at 850 F/g, however on average, over all scan rates, LCO maintains the higher capacitances around 150 F/g. The decline of capacitance with increasing scan rates could be attributed to an inadequate time period for the faradic redox reaction completion.

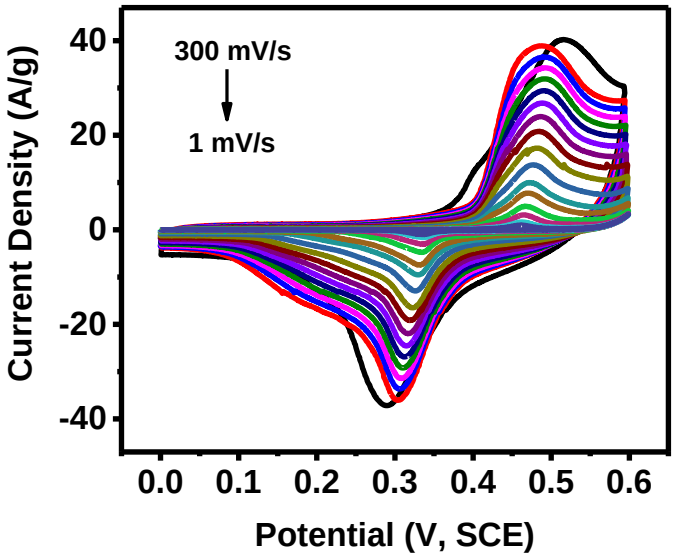

Figure 3.41: Cyclic voltammograms of LCO at various scan rates

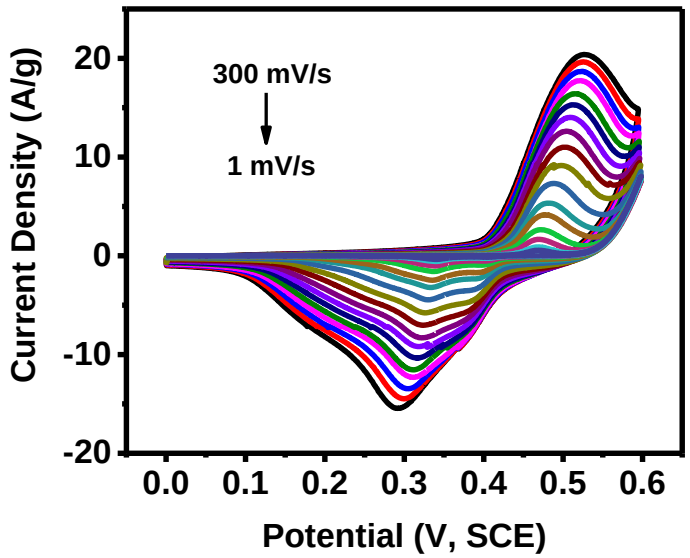

Figure 3.42: Cyclic voltammograms of LFO at various scan rates

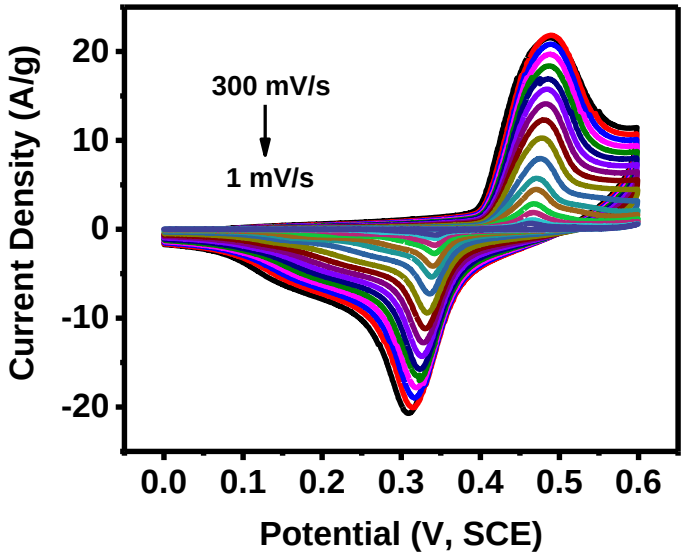

Figure 3.43: Cyclic voltammograms of LMO at various scan rates

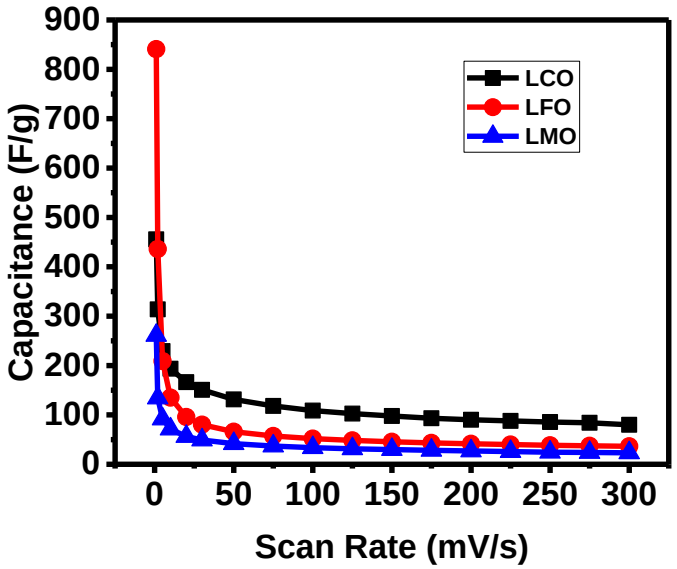

Figure 3.44: Specific capacitance of perovskites at various scan rates

3.4.2 Galvanostatic charge discharge:

The perovskite metal oxides were then analyzed with galvanostatic charge-discharge measurements over current densities between 0.5 and 20 A/g (Figure 3.45-47). The GCD curve shapes corroborate the faradic mechanism established from the CV curves. The discharge times were observed to decrease as current density increased, which would again be attributed to insufficient time for redox to occur. Specific capacitance based on GCD curves were calculated according to the following equation:

$$C_{sp} = \frac{I\Delta t}{m\Delta V} \tag{9}$$

where I is the discharge current (A), Δt is the discharge time (s), m is the mass (g) of the

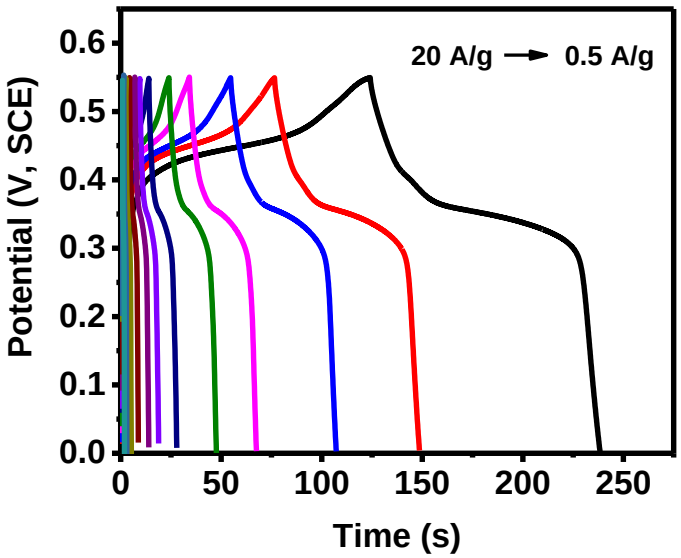

Figure 3.45: GCD curves for LCO at a range of current densities

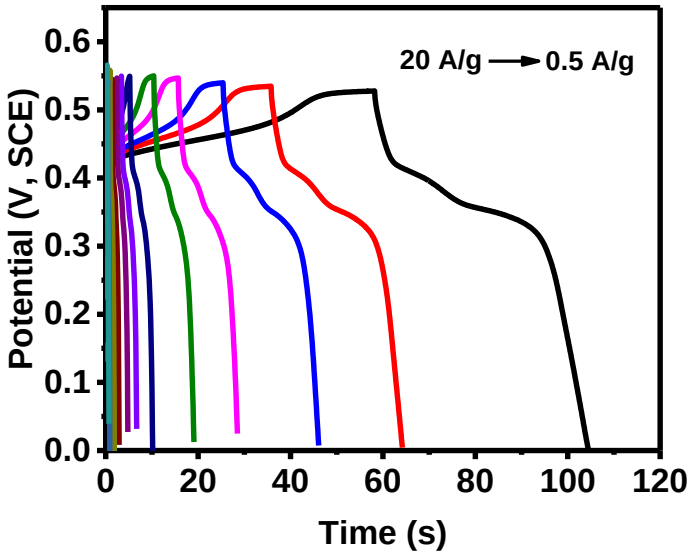

Figure 3.46: GCD curves for LFO at a range of current densities

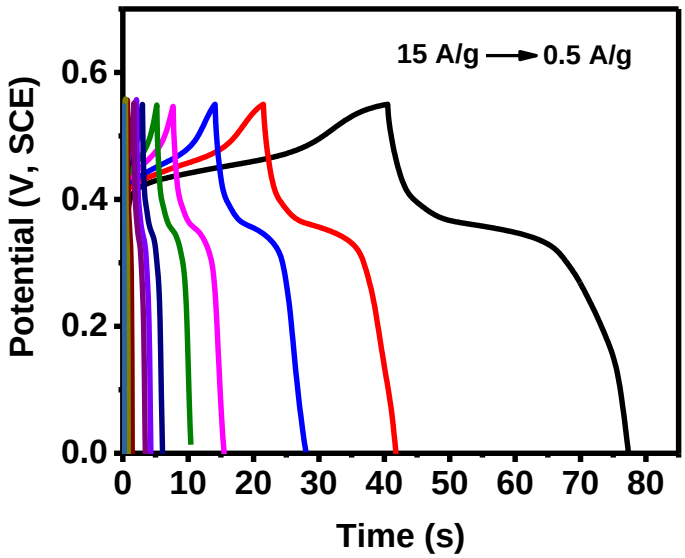

Figure 3.47: GCD curves for LMO at a range of current densities

perovskite material, and ΔV is the potential window (V).[39] In Figures 3.48-3.50, the specific capacitance of all the materials was observed to decrease upon shifting to higher current densities, as a result of a short interaction time frame. Although LFO achieved higher capacitance at the lowest current density, the capacitance quickly drops as current density increases compared to LCO that maintains high capacitances longer.

3.4.3 Stability measurements:

To better understand the effects of repeated charging and discharging on the ability of LCO to store energy, the electrode was cycled at 1.5 A/g over a 0 to 0.55 V potential range for 5000 cycles. Capacitance retention of LFO and LMO remained relatively constant throughout the entire 5000 cycles as seen in Figures 3.52 and 3.53, respectively.

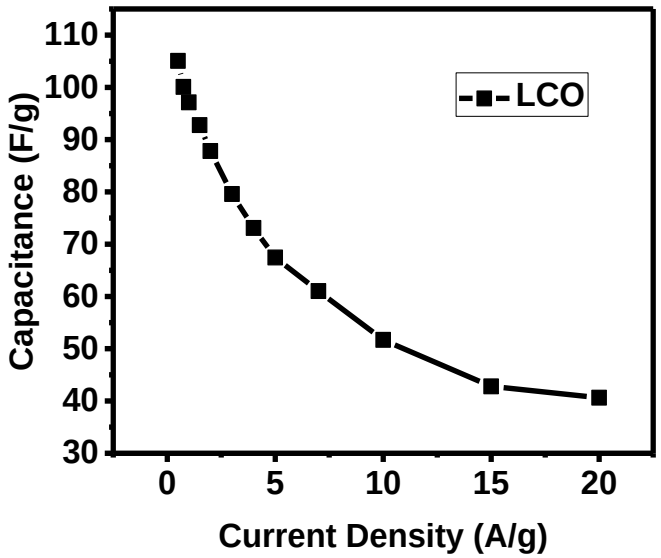

Figure 3.48: Specific capacitance curve from GCD curves for lanthanum cobaltite

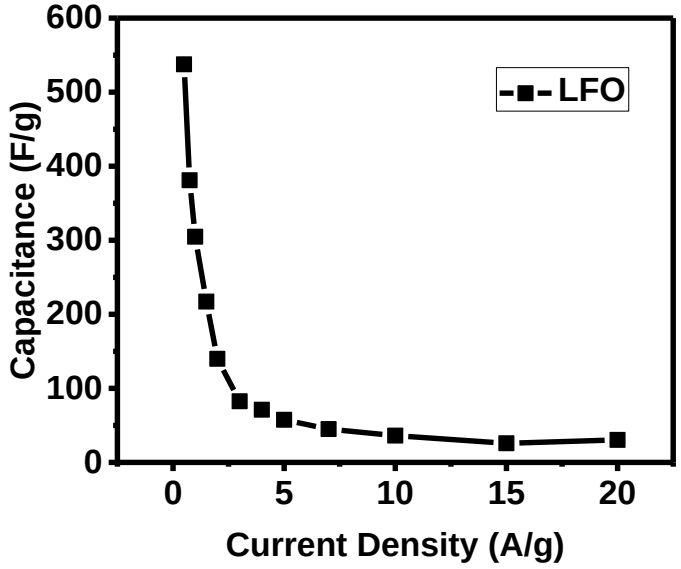

Figure 3.49: Specific capacitance curve from GCD curves for lanthanum ferrite

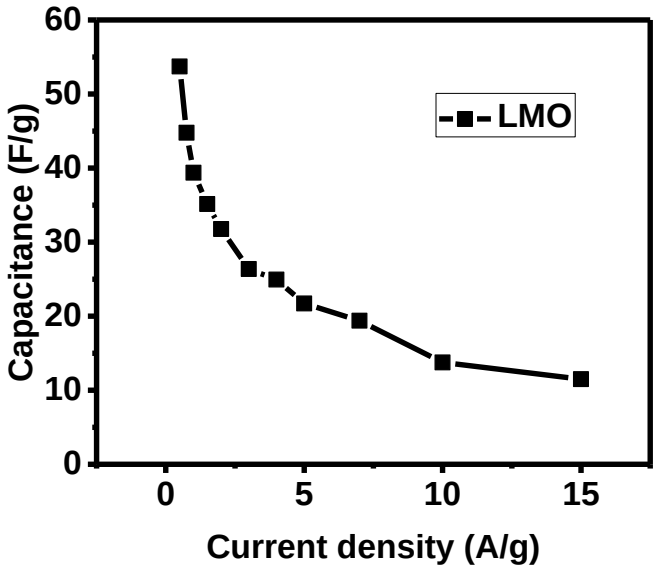

Figure 3.50: Specific capacitance curve from GCD curves for lanthanum manganite

However, the ability of LCO to retain its capacitance was shown to increase by up to 60% as seen in Figure 3.51. This occurrence has been noted in other supercapacitor materials and likely stems from prolonged wetting of the porous material over long experiment time.[40]

Coulombic efficiency of the materials remained stable and from the insets the charge discharge time increased slightly from the first ten cycles to the last ten for the perovskites, with LFO as the exception. On the whole, all three perovskite metal oxides proved to remain adequately stable and function well as supercapacitor electrode materials.

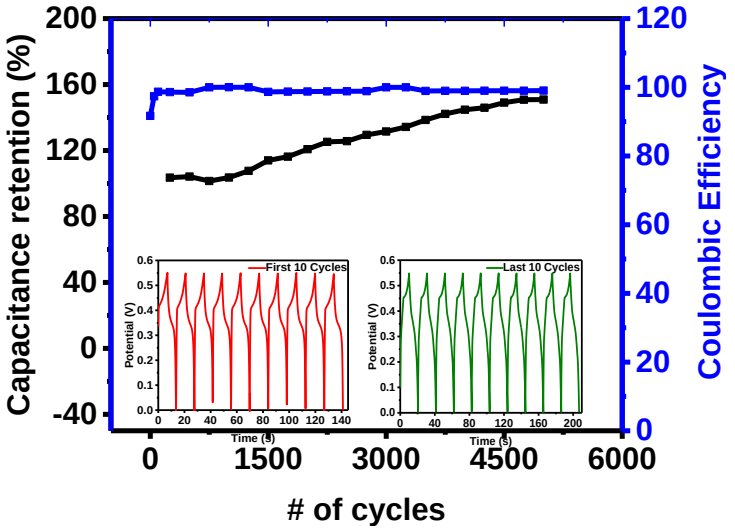

Figure 3.51: Capacitance retention and efficiency of LCO electrode from GCD cycling

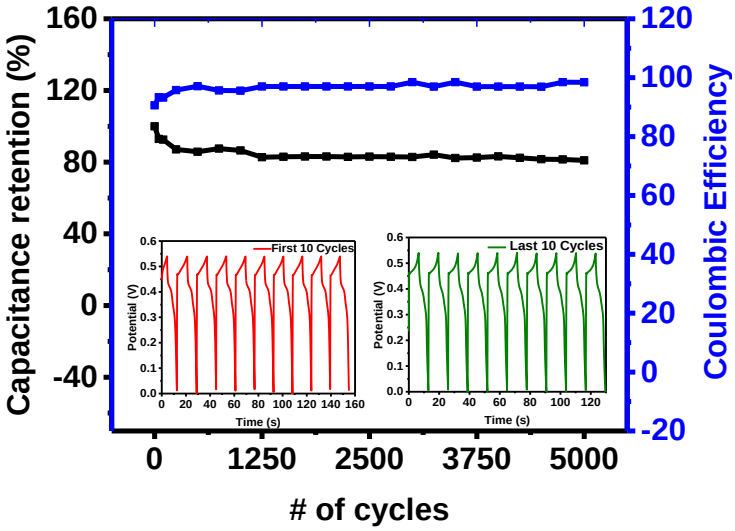

Figure 3.52: Capacitance retention and efficiency of LFO electrode from GCD cycling

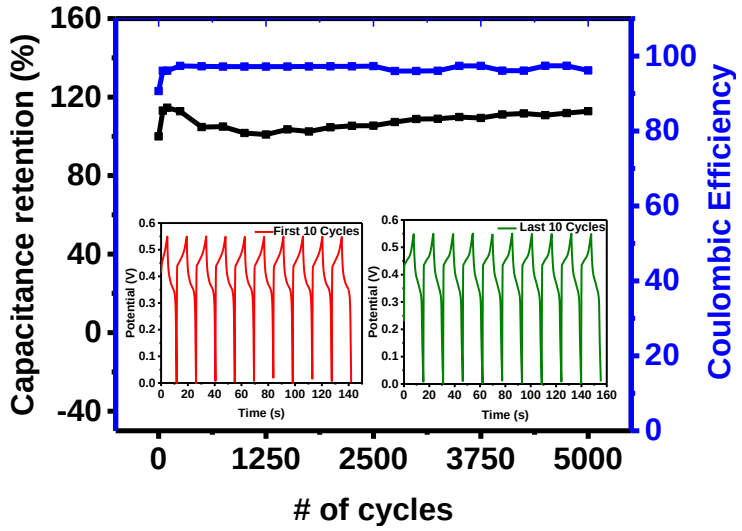

Figure 3.53: Capacitance retention and efficiency of LMO electrode from GCD cycling

3.5 Effects of structure directing agents:

3.5.1: Structure directing agents:

In the synthetic route, outlined by Kim et al., glycine was employed as a structure directing agent (SDA) or chelating agent.[41] Transition metal nitrates, used as starting materials, dissociate in deionized water forming water complexed metals in solution. Glycine reacts with ammonium and replaces the complexed water ligands afforded by the thermodynamic stability of polydentate ligands than the monodentate water molecules, depicted in Figure 3.54.[42] During the hydrothermal reaction process, the metal complexes migrate, assemble and grow into the perovskite crystal structure in a form of the Ostwald ripening process.[43] The use of PVP is noted as a surfactant which acts as a particle size modulator, as particle size varies with amount of PVP.[41,44]

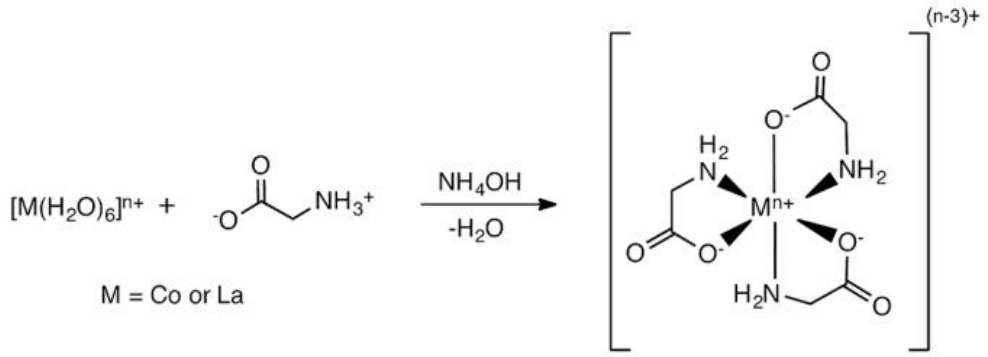

Figure 3.54: Chelating effect of glycine.[41] Reprinted with permission from ACS publications

Based on SEM imagery, the initial synthetic process was successful with the formation of nanosphere particles for LCO, and moderate LFO nanosphere formation. LMO results were less than desired in the formation of distinct nano-sized spherical particles. In an attempt to find an SDA that would achieve the desired nanostructures for all three perovskites, glycine was replaced with citric acid. Citric acid has been widely used for the synthesis of perovskites, especially in the sol-gel synthesis method.[27,45,46,47] The hydrothermal process for synthesis with citric acid is shown in the following reaction sequence:

$$La(NO_3)_3 \rightarrow La^{3+} + 3NO^{3-} \quad (10)$$

$$M(NO_3)_3 \rightarrow M^{3+} + 3OH^- \rightarrow M(OH)_3 \quad (11)$$

$$La^{3+} + C_6O_7H_8 \rightarrow [C_6O_7H_5]^{3-}\ La^{3+} + 3H^+ \quad (12)$$

$$[C_6O_7H_5]^{3-}\ La^{3+} + 3OH^- \rightarrow La(OH)_3 + [C_6O_7H_5]^{3-} \quad (13)$$

$$La(OH)_3 + M(OH)_3 \rightarrow LaMO_3 + 3H_2O \quad (14)$$

where M denotes the B-site transition metal (Co, Fe, Mn).[48]

3.5.2: X-ray diffraction comparison:

XRD spectral comparisons of each of the citric acid synthesized perovskite materials with the glycine method are shown in Figures 3.55, 3.56, and 3.57. Notable changes in spectra, aside from peak intensity, are the shift or removal of the (202) and (024) peaks at ~41˚ and ~48˚, respectively for LCO. In the LFO spectra comparison, the La_2O_3

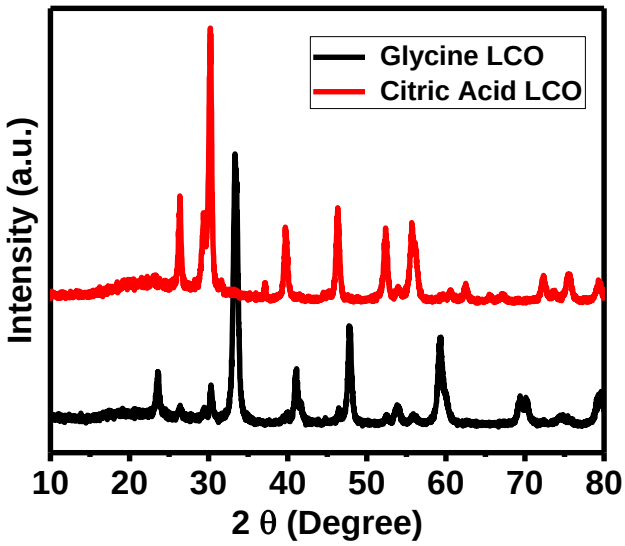

Figure 3.55: XRD of LCO synthesis method comparison

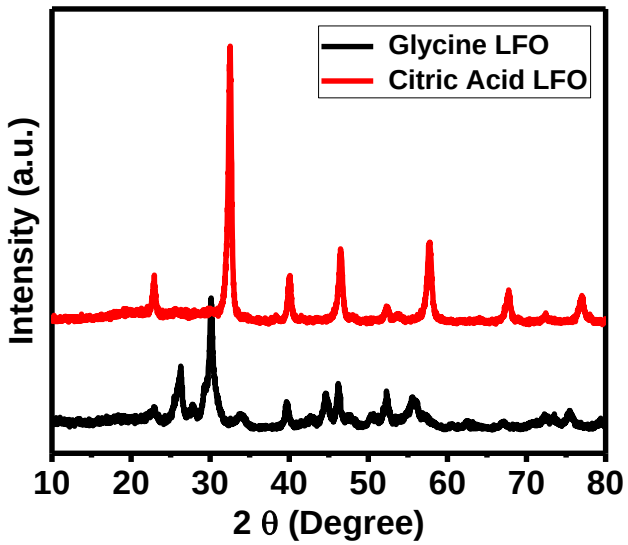

Figure 3.56: XRD of LFO synthesis method comparison

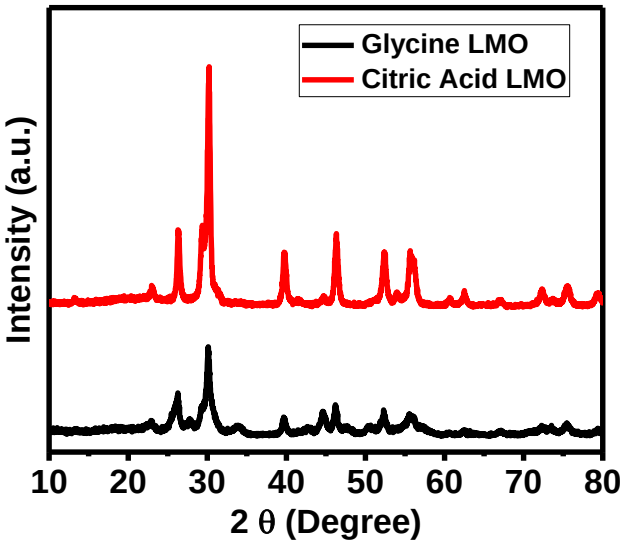

Figure 3.57: XRD of LMO synthesis method comparison

peaks were noticeable absent and sharper, more defined peaks were observed. Minimal change in LMO spectra were detected. Based on XRD spectra and SEM imaging, glycine as a chelating agent interacted more favorable with lanthanum cobaltite in forming discrete small spherical particles. Citric acid on the other hand, directed the formation of lanthanum ferrite more advantageously than the other materials. Neither glycine, nor citric acid directed the formation of nanoscopic spherical particles of lanthanum manganite. Potential explanation of lack of change in interaction with manganese could reside with ionic radii of Co^{3+}, Fe^{3+} and Mn^{2+}, which are 68.5, 69.0 and 81.0 pm, respectively.[49] Cobalt and iron which are roughly the same size showed better particle formation with glycine and citric acid chelation as depicted in Figure 3.54 and 3.58. Further investigation to whether a

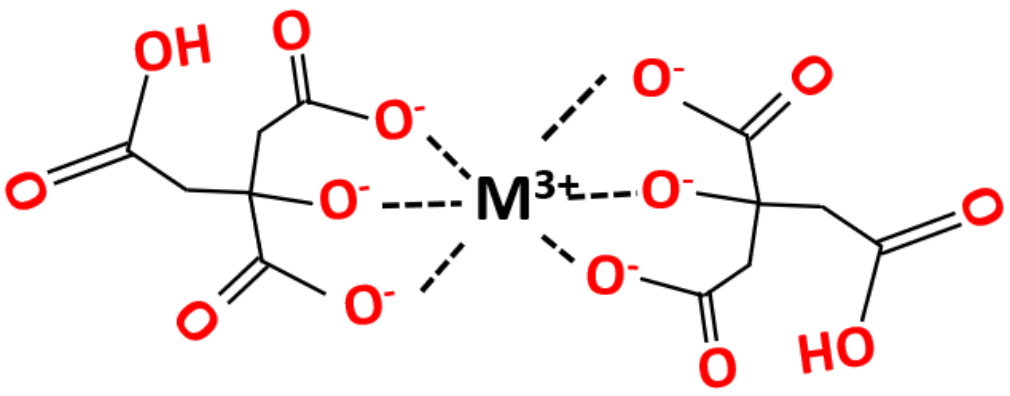

Figure 3.58: Coordination of citric acid and M^{3+} transition metal

chelating agent better suited to interact with Mn^{2+} could produce distinct nanospheres is needed.

3.5.3: Effects on OER:

Analysis toward the OER were conducted with the perovskite materials synthesize with citric acid. LSV with the same experimental parameters as with glycine showed improvement in overpotential reduction in LFO and LMO, but an increase in overpotential in LCO as shown in Figures 3.59, 3.60 and 3.61. Citric acid appeared to negatively affect LCO which is likely connected to the shift in structure noted in the XRD spectra. LMO

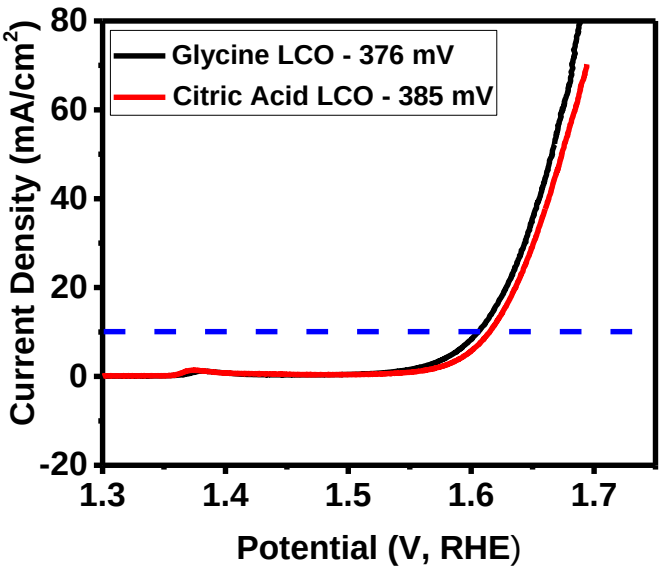

Figure 3.59: LCO overpotential comparison from LSV

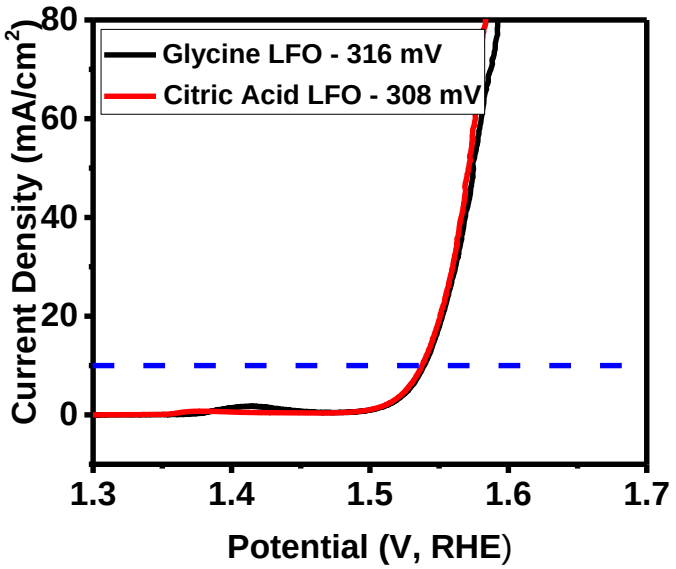

Figure 3.60: LFO overpotential comparison from LSV

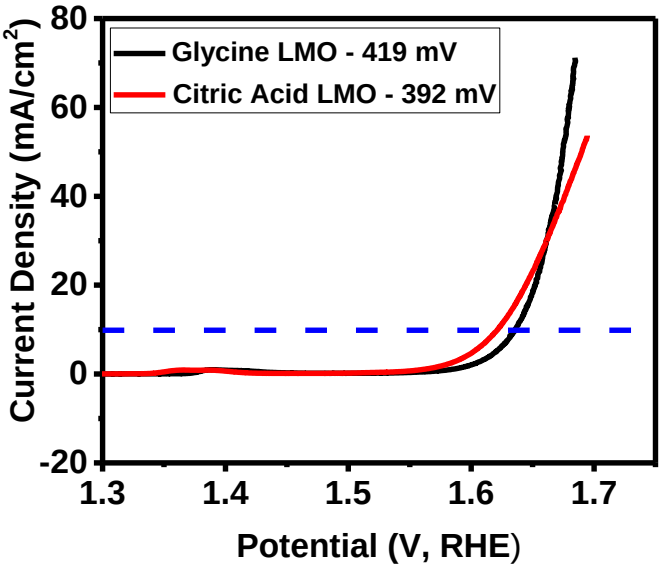

Figure 3.61: LMO overpotential comparison from LSV

however, showed an overpotential reduction of 27 mV. This occurrence may be linked to an increase in crystallinity. Spectral peaks appeared to become sharper compared to the broader peaks from glycine which indicates the a more crystalline material. EIS Nyquist plots at 0 (Figures 3.62-3.64) show greater charge transfer resistance from citric acid in all materials. At 0.5V in Figure 3.65, 3.66, and 3.67, again show increased resistance in the materials synthesized by citric acid, except LMO. Charge transfer resistance decreases from 100 ohms to ~50 ohms.

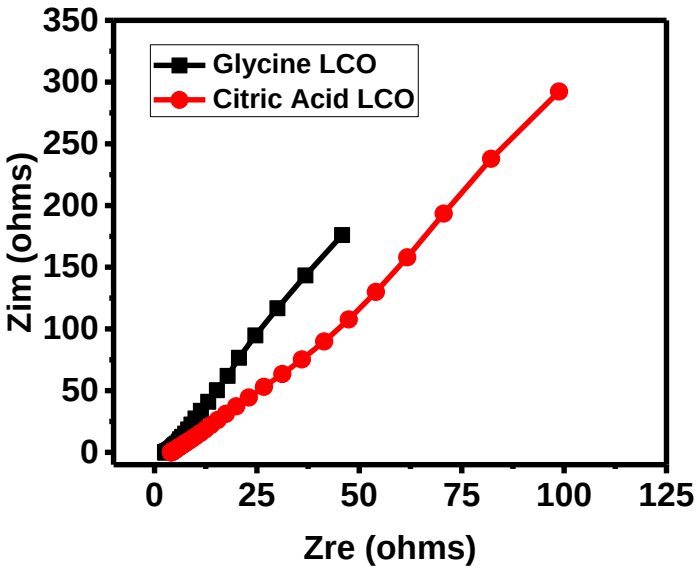

Figure 3.62: LCO EIS Nyquist comparison at 0V

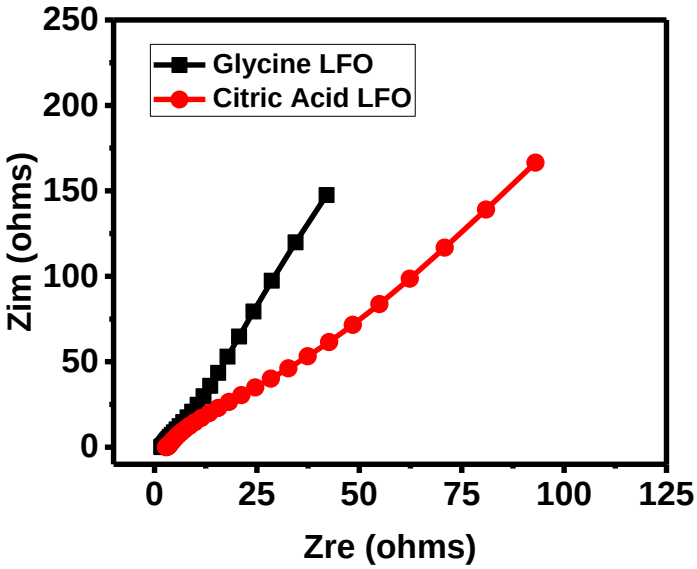

Figure 3.63: LFO EIS Nyquist comparison at 0V

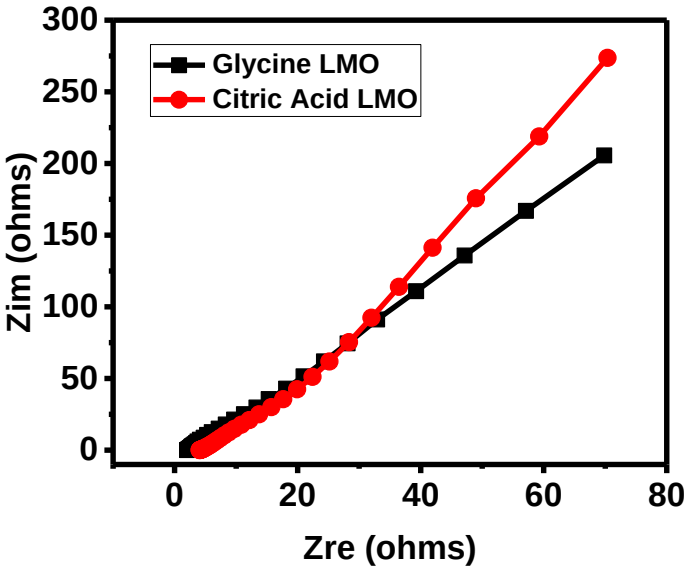

Figure 3.64: LMO EIS Nyquist comparison at 0V

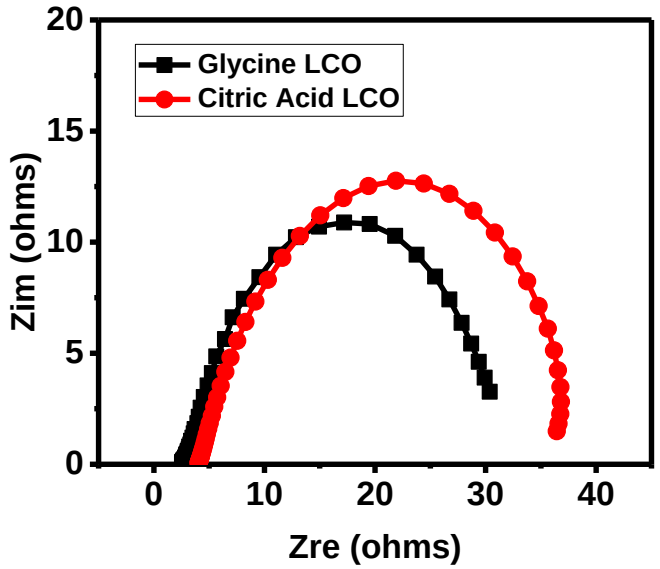

Figure 3.65: LCO EIS Nyquist comparison at 0.5V

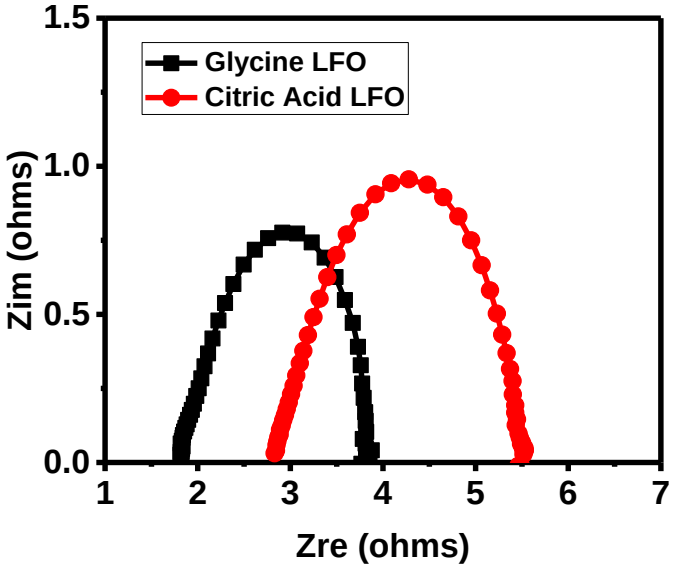

Figure 3.66: LFO EIS Nyquist comparison at 0.5V

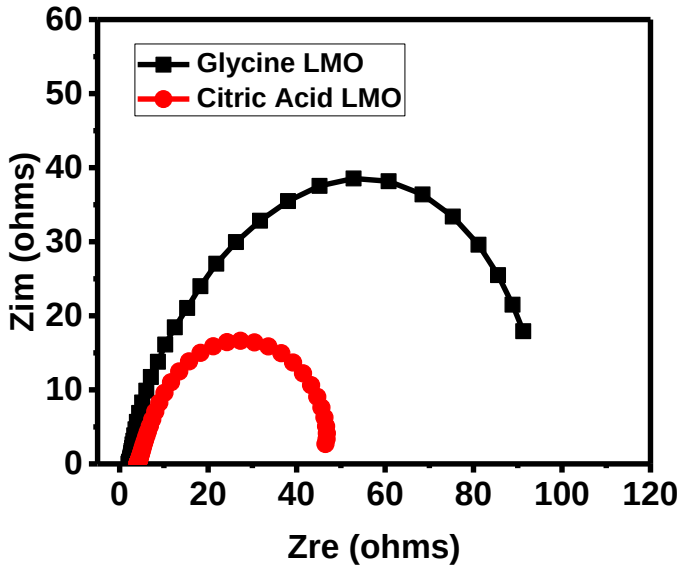

Figure 3.67: LMO EIS Nyquist comparison at 0.5V

CHAPTER IV

CONCLUSION

Three lanthanum-based perovskite metal oxides were synthesized using glycine and PVP to facilitate the production of microscopic and nanoscopic electrocatalytic materials through a hydrothermal reaction and a two-step calcination process. The resulting LCO, LFO, and LMO were characterized by XRD and SEM to investigate the materials' structural features. Each metal oxide was then analyzed as multifunctional materials for effectiveness toward OER, HER and as an energy storage supercapacitor. LFO exhibited the lowest overpotential of 316 mV toward OER compared with LCO and LMO. With respect to HER, LMO produced the lowest overpotential of 176 mV as well as proved to be quite structurally stable over extended periods of use. LCO was found to be the most effective energy storage material for use as a supercapacitor with an average specific capacitance of 150 F/g. Although it was found that each of the perovskite metal oxides performed better in different areas, it is worth noting that all three were capable of performing all three functions as a multifunctional material.

Additional research was conducted to investigate the affect of replacing structure directing chelating agent on perovskite metal oxide structure and electrocatalytic properties. Glycine was replaced with citric acid and ammonium was removed in the synthetic method. The new synthesis was shown to improve the XRD spectra of LFO by

removing La_2O_3 peaks and sharpening of crystalline peaks. LCO showed a shifting and removal of peaks. LMO spectra showed minimal change with slightly sharper peaks due to the citric acid. Electrocatalytic abilities toward the OER the most change in a reduction of 27 mV in overpotential for LMO. LFO had a small reduction in overpotential whereas LCO gained overpotential compared to the glycine method. EIS charge transfer resistance was increased in all materials at both 0V and 0.5V except for LMO at 0.5V. Resistance was decreased by ~50 ohms.

Results suggest that these lanthanum-based perovskite metal oxides have the ability to operate as multifunctional electrodes for water splitting and supercapacitor energy storage devices. Further investigation toward a suitable SDA for manganese and fine-tuning structural properties is need to achieve greater efficiency in all three materials' electrocatalytic properties.

References

(1) UNFCCC. Conference of the Parties (COP). ADOPTION OF THE PARIS AGREEMENT - Conference of the Parties COP 21. *Adopt. Paris Agreement. Propos. by Pres.* **2015**, *21932* (December), 32.

(2) Allen, A.; Anenberg, S. C.; Baker, J.; Barker, C.; Baumann, M.; Beach, R.; Belova, A.; Benishek, C.; Bierman, V. J.; Bierwagen, B.; et al. Multi-Model Framework for Quantitative Sectoral Impacts Analysis. **2017**, May.

(3) Wiser, R.; Bolinger, M.; Barbose, G.; Darghouth, N.; Hoen, B.; Mills, A.; Rand, J.; Millstein, D.; Porter, K.; Widiss, R.; et al. Revolution… Now: The Future Arrives for Five Clean Energy Technologies - 2016 Update. **2016**, September, 1–30.

(4) Anantharaj, S.; Ede, S. R.; Sakthikumar, K.; Karthick, K.; Mishra, S.; Kundu, S. Recent Trends and Perspectives in Electrochemical Water Splitting with an Emphasis on Sulfide, Selenide, and Phosphide Catalysts of Fe, Co, and Ni: A Review. *ACS Catal.* **2016**, *6* (12), 8069–8097.

(5) You, B.; Sun, Y. Innovative Strategies for Electrocatalytic Water Splitting. *Acc. Chem. Res.* **2018**, *51* (7), 1571–1580.

(6) Sapountzi, F. M.; Gracia, J. M.; Weststrate, C. J. (Kee.-J.; Fredriksson, H. O. A.; Niemantsverdriet, J. W. (Hans. Electrocatalysts for the Generation of Hydrogen, Oxygen and Synthesis Gas. *Prog. Energy Combust. Sci.* **2017**, *58*, 1–35.

(7) Baglio, V.; Ornelas, R.; D'Urso, C.; Antonucci, V.; Di Blasi, A.; Orozco, G.; Meas, Y.; Arriaga, L. G.; Beltran, D.; Arico', A. S.; et al. Preparation and Evaluation of RuO_2–IrO_2, IrO_2–Pt and IrO_2–Ta_2O_5 Catalysts for the Oxygen Evolution Reaction in an SPE Electrolyzer. *J. Appl. Electrochem.* **2008**, *39* (2), 191–196.

(8) Xu, X.; Su, C.; Zhou, W.; Zhu, Y.; Chen, Y.; Shao, Z. Co-Doping Strategy for Developing Perovskite Oxides as Highly Efficient Electrocatalysts for Oxygen Evolution Reaction. *Adv. Sci.* **2015**, *3* (2), 1–6.

(9) Fabbri, E.; Habereder, A.; Waltar, K.; Kötz, R.; Schmidt, T. J. Developments and Perspectives of Oxide-Based Catalysts for the Oxygen Evolution Reaction. *Catal. Sci. Technol.* **2014**, *4* (11), 3800–3821.

(10) Otagawa, T.; Bockris, J. O. Oxygen Evolution on Perovskites. *J. Phys. Chem* **1983**, *87* (15), 2960–2971.

(11) Schmidt, T. J.; Marzari, N.; El Kazzi, M.; Haumont, R.; Castelli, I. E.; Fabbri, E.; Nachtegaal, M.; Cheng, X. Oxygen Evolution Reaction on $La_{1-x}Sr_xCoO_3$ Perovskites: A Combined Experimental and Theoretical Study of Their Structural, Electronic, and Electrochemical Properties . *Chem. Mater.* **2015**, *27* (22), 7662–7672.

(12) Thirumalairajan, S.; Girija, K.; Hebalkar, N. Y.; Mangalaraj, D.; Viswanathan, C.; Ponpandian, N. Shape Evolution of Perovskite $LaFeO_3$ nanostructures: A Systematic Investigation of Growth Mechanism, Properties and Morphology Dependent Photocatalytic Activities. *RSC Adv.* **2013**, *3* (20), 7549–7561.

(13) Sunarso, J.; Zhong, Y.; Shao, Z.; Zhou, W.; Zhu, Y. Phosphorus-Doped Perovskite Oxide as Highly Efficient Water Oxidation Electrocatalyst in Alkaline Solution. *Adv. Funct. Mater.* **2016**, *26* (32), 5862–5872.

(14) Wang, Y.; Cheng, H. P. Oxygen Reduction Activity on Perovskite Oxide Surfaces:

A Comparative First-Principles Study of $LaMnO_3$, $LaFeO_3$, and $LaCrO_3$. *J. Phys. Chem. C* **2013**, *117* (5), 2106–2112.
(15) Bockris, J. O. M.; Minevski, Z. S. Electrocatalysis: A Futuristic View. *Int. J. Hydrogen Energy* **1992**, *17* (6), 423–444.
(16) Nyamdavaa, E.; Altantsog, P.; Uyanga, E.; Bumaa, B.; Chen, T. Y.; Lee, C. H.; Sevjidsuren, G.; Sangaa, D. Crystal Structure Study of Perovskite-Type $LaCoO_3$ Electro-Catalyst Synthesized by Pechini Method. *Proc. 6th Int. Forum Strateg. Technol. IFOST 2011* **2011**, *1* (3), 61–64.
(17) Batdemberel, G.; Bulgan, G.; Dinnebier, R. E.; Munkhbaatar, P.; Sangaa, D.; Chadraabal, S. Rietveld Refinement Of Nanostructural $LaMnO_3$ Perovskite- Type Manganite. *IEEE - IFOST Proc.* **2010**, 3–5.
(18) Tan, W.; Bowring, A. R.; Meng, A. C.; McGehee, M. D.; McIntyre, P. C. Thermal Stability of Mixed Cation Metal Halide Perovskites in Air. *ACS Appl. Mater. Interfaces* **2018**, *10* (6), 5485–5491.
(19) Zhang, H.; Li, N.; Li, K.; Xue, D. Structural Stability and Formability of ABO_3-Type Perovskite Compounds. *Acta Crystallogr. Sect. B Struct. Sci.* **2007**, *63* (6), 812–818.
(20) Stevenson, K. J.; Dai, S.; Mefford, J. T.; Hardin, W. G.; Johnston, K. P. Anion Charge Storage through Oxygen Intercalation in $LaMnO_3$ Perovskite Pseudocapacitor Electrodes. *Nat. Mater.* **2014**, *13* (7), 726–732.
(21) Salunkhe, R. R.; Kaneti, Y. V.; Yamauchi, Y. Metal-Organic Framework-Derived Nanoporous Metal Oxides toward Supercapacitor Applications: Progress and Prospects. *ACS Nano* **2017**, *11* (6), 5293–5308.
(22) Nan, H.; Hu, X.; Tian, H. Recent Advances in Perovskite Oxides for Anion-Intercalation Supercapacitor: A Review. *Mater. Sci. Semicond. Process.* **2019**, *94* (January), 35–50.
(23) Mastragostino, M.; Soavi, F.; Arbizzani, C. Electrochemical Supercapacitors. *Adv. Lithium-Ion Batter.* **2006**, 481–505.
(24) Shao, L.; Qian, X.; Wang, X.; Li, H.; Yan, R.; Hou, L. Low-Cost and Highly Efficient $CoMoS_4$/$NiMoS_4$-Based Electrocatalysts for Hydrogen Evolution Reactions over a Wide PH Range. *Electrochim. Acta* **2016**, *213*, 236–243.
(25) Zhang, Y.; Chao, S.; Wang, X.; Han, H.; Bai, Z.; Yang, L. Hierarchical Co_9S_8 Hollow Microspheres as Multifunctional Electrocatalysts for Oxygen Reduction, Oxygen Evolution and Hydrogen Evolution Reactions. *Electrochim. Acta* **2017**, *246*, 380–390.
(26) Islam, M.; Jeong, M.-G.; Ghani, F.; Jung, H.-G. Micro Emulsion Synthesis of $LaCoO_3$ Nanoparticles and Their Electrochemical Catalytic Activity . *J. Electrochem. Sci. Technol.* **2016**, *6* (4), 121–130.
(27) Li, Y.; Xue, L.; Fan, L.; Yan, Y. The Effect of Citric Acid to Metal Nitrates Molar Ratio on Sol-Gel Combustion Synthesis of Nanocrystalline $LaMnO_3$ Powders. *J. Alloys Compd.* **2009**, *478* (1–2), 493–497.
(28) Chao, R.; Munprom, R.; Petrova, R.; Gerdes, K.; Kitchin, J. R.; Salvador, P. A. Structure and Relative Thermal Stability of Mesoporous (La, Sr) MnO_3 powders Prepared Using Evaporation-Induced Self-Assembly Methods. *J. Am. Ceram. Soc.* **2012**, *95* (7), 2339–2346.
(29) Li, Z.; Zhang, W.; Yuan, C.; Su, Y. Controlled Synthesis of Perovskite Lanthanum

Ferrite Nanotubes with Excellent Electrochemical Properties. *RSC Adv.* **2017**, *7* (21), 12931–12937.
(30) Matsumoto, Y.; Sato, E. Electrocatalytic Properties of Transition Metal Oxides for Oxygen Evolution Reaction. *Mater. Chem. Phys.* **1986**, *14* (5), 397–426.
(31) Bockris, J. O'M., Minevski, Z. S. ELECTROCATALYSIS : PAST , PRESENT AND FUTURE. *Electrochim. Acta* **1994**, *39* (11), 1471–1479.
(32) Giménez, S.; Bisquert, J. *Photoelectrochemical Solar Fuel Production: From Basic Principles to Advanced Devices*; 2016.
(33) Shinagawa, T.; Garcia-Esparza, A. T.; Takanabe, K. Insight on Tafel Slopes from a Microkinetic Analysis of Aqueous Electrocatalysis for Energy Conversion. *Sci. Rep.* **2015**, *5* (September), 1–21.
(34) Zhu, Y.; Chen, Z. G.; Zhou, W.; Jiang, S.; Zou, J.; Shao, Z. An A-Site-Deficient Perovskite Offers High Activity and Stability for Low-Temperature Solid-Oxide Fuel Cells. *ChemSusChem* **2013**, *6* (12), 2249–2254.
(35) Su, H. Y.; Sun, K. DFT Study of the Stability of Oxygen Vacancy in Cubic ABO_3 perovskites. *J. Mater. Sci.* **2015**, *50* (4), 1701–1709.
(36) Yang, M.; Xu, A.; Du, H.; Sun, C.; Li, C. Removal of Salicylic Acid on Perovskite-Type Oxide $LaFeO_3$ Catalyst in Catalytic Wet Air Oxidation Process. **2007**, *139*, 86–92.
(37) Brousse, T.; Bélanger, D.; Long, J. W. To Be or Not To Be Pseudocapacitive? *J. Electrochem. Soc.* **2015**, *162* (5), A5185–A5189.
(38) Alqahtani, D. M.; Zequine, C.; Ranaweera, C. K.; Siam, K.; Kahol, P. K.; Poudel, T. P.; Mishra, S. R.; Gupta, R. K. Effect of Metal Ion Substitution on Electrochemical Properties of Cobalt Oxide. *J. Alloys Compd.* **2019**, *771*, 951–959.
(39) Arjun, N.; Pan, G. T.; Yang, T. C. K. The Exploration of Lanthanum Based Perovskites and Their Complementary Electrolytes for the Supercapacitor Applications. *Results Phys.* **2017**, *7*, 920–926.
(40) Zequine, C.; Ranaweera, C. K.; Wang, Z.; Singh, S.; Tripathi, P.; Srivastava, O. N.; Gupta, B. K.; Ramasamy, K.; Kahol, P. K.; Dvornic, P. R.; et al. High per Formance and Flexible Supercapacitors Based on Carbonized Bamboo Fibers for Wide Temperature Applications. *Sci. Rep.* **2016**, *6* (May), 1–10.
(41) Kim, J.; Chen, X.; Shih, P. C.; Yang, H. Porous Perovskite-Type Lanthanum Cobaltite as Electrocatalysts toward Oxygen Evolution Reaction. *ACS Sustain. Chem. Eng.* **2017**, *5* (11), 10910–10917.
(42) Miessler, Gary L., Fischer, Paul J., Tarr, D. A. *Inorganic Chemistry*, Fifth Edit.; Pearson, 2014.
(43) Yang, H. G.; Zeng, H. C. Preparation of Hollow Anatase TiO_2 Nanospheres via Ostwald Ripening . *J. Phys. Chem. B* **2004**, *108* (11), 3492–3495.
(44) Qin, C.; Li, Z.; Chen, G.; Zhao, Y.; Lin, T. Fabrication and Visible-Light Photocatalytic Behavior of Perovskite Praseodymium Ferrite Porous Nanotubes. *J. Power Sources* **2015**, *285*, 178–184.
(45) Lertpanyapornchai, B.; Yokoi, T.; Ngamcharussrivichai, C. Citric Acid as Complexing Agent in Synthesis of Mesoporous Strontium Titanate via Neutral-Templated Self-Assembly Sol-Gel Combustion Method. *Microporous Mesoporous Mater.* **2016**, *226*, 505–509.
(46) Hernández, E.; Sagredo, V.; Delgado, G. E. Synthesis and Magnetic

Characterization of $LaMnO_3$ Nanoparticles. *Rev. Mex. Fis.* **2015**, *61* (3), 166–169.
(47) Peng, K.; Fu, L.; Yang, H.; Ouyang, J. Perovskite $LaFeO_3$/Montmorillonite Nanocomposites: Synthesis, Interface Characteristics and Enhanced Photocatalytic Activity. *Sci. Rep.* **2016**, *6* (January), 1–10.
(48) Dhinesh Kumar, R.; Jayavel, R. Facile Hydrothermal Synthesis and Characterization of $LaFeO_3$ Nanospheres for Visible Light Photocatalytic Applications. *J. Mater. Sci. Mater. Electron.* **2014**, *25* (9), 3953–3961.
(49) Shannon, R. D. Revised Effective Ionic Radii and Systematic Studies of Interatomic Distances in Halides and Chalcogenides. *Acta Crystallogr. Sect. A* **2002**, *32* (5), 751–767..